Spring 2022

The Role of Ions in Irradiated Astrophysical O_2 Ice

Kristen J. Darnell
San Jose State University

THE ROLE OF IONS IN IRRADIATED ASTROPHYSICAL O_2 ICE

A Thesis

Presented to

The Faculty of the Department of Physics and Astronomy

San José State University

In Partial Fulfillment

of the Requirements for the Degree

Master of Science

by

Kristen J. Darnell

May 2022

The Designated Thesis Committee Approves the Thesis Titled

THE ROLE OF IONS IN IRRADIATED ASTROPHYSICAL O_2 ICE

by

Kristen J. Darnell

APPROVED FOR THE DEPARTMENT OF PHYSICS AND ASTRONOMY

SAN JOSÉ STATE UNIVERSITY

May 2022

Thomas Madura, Ph.D.	Department of Physics and Astronomy
Christopher Shingledecker, Ph.D.	Department of Physics and Astronomy Benedictine College
Michael Kaufman, Ph.D.	Department of Physics and Astronomy
Monika Kress, Ph.D.	Department of Physics and Astronomy

ABSTRACT

THE ROLE OF IONS IN IRRADIATED ASTROPHYSICAL O_2 ICE

by Kristen J. Darnell

Cosmic ices contain ions produced by irradiation from cosmic rays and UV photons, yet solid-phase ion-ice reactions are currently ignored in all astrochemical models, even though gas-phase ion-molecule reactions are arguably the single-most important class of reactions in astrochemistry. Thus, developing a model that includes solid-phase ion-ice reactions is essential to accurately model interstellar ice chemistry, especially given the recent launch of the James Webb Space Telescope. To fill this gap, we have compiled a solid-phase chemical network for use in a rate-based irradiated ice astrochemical model which, for the first time, includes ionic species produced via the photoionization of the ice. Using this network, we simulated the photo-irradiation of a pure O_2 ice and constrained the photolysis rates through direct comparison with experimental data. The fit of the model is in qualitative agreement with the experimental findings to give a general idea of what ionic chemistry occurs in irradiated ices. Our preliminary results indicate that ion-neutral chemistry contributes significantly more to solid phase reactivity than previously assumed. As in the gas-phase, solid-phase ion-ice reactions are very efficient and, indeed, become the dominant formation routes for the neutral species in our network.

ACKNOWLEDGMENTS

The story of this thesis begins long before I started graduate school. It starts long before I started college. My journey to this thesis started with Mr. Richard Brown, my middle school science teacher, who valiantly and patiently tried to distill the essence of nuclear physics for a 13-year-old who desperately wanted to understand. It was then that I decided to study science. Since that moment, I have received support from so many wonderful people as I followed my fascination with physics through high school, college, and into graduate school.

As a first year master's student, I still had not decided which element of physics I wanted to devote my career to. Dr. Michael Kaufman, despite his busy schedule as the Dean of Science, took the time to talk to me about his research in astrochemistry, and I was immediately intrigued. I then had the opportunity to work with Dr. Agata Karska at Nicolaus Copernicus University on mapping regions of stellar formation in the outer galaxy. She invited me to participate in the Torun Astrophysics, Spectroscopy, and Quantum Chemistry School (TASQ), where I received a more thorough introduction to many of the topics and key players in astrochemistry, and I knew this was the field I wanted to pursue.

Back at SJSU, I found myself indebted to Dr. Thomas Madura. Even though his research did not focus on astrochemistry, he offered to reach out to his professional network to help me find the support I needed to work on a project I was truly passionate about. I thus came into collaboration with Dr. Christopher Shingledecker at Benedictine College, who has been the most incredible supervisor, research advisor, and mentor through my graduate studies. I have enjoyed every second of this project (even the tedious ones!) and I am so proud of the work I have done under his guidance.

So thank you to the people who have helped me on my journey.

Thank you Mr. Brown for providing the initial sparks of what would become a lifelong passion for science.

Thank you Dr. Karska for giving me my first taste of astrochemistry research.

Thank you Dr. Kress for helping me find balance between my coursework, research, and teaching responsibilities.

Thank you Dr. Kaufman for taking the time out of your busy schedule for that career-changing conversation, and for encouraging me to pursue the wonderful conference and travel opportunities I have enjoyed since then.

Thank you Dr. Madura for your support and guidance throughout this project. Your willingness to explore outside your field has allowed me to accomplish something I'm truly proud of.

Thank you Dr. Shingledecker for the incredible mentoring you have given me. I have truly enjoyed the hours we've spent pouring over spreadsheets, code and plots.

I also owe thanks to many people outside of the university. Without the support of my friends and family, this thesis would still be a disjointed, incomprehensible jumble of thoughts and references. I say thank you to:

Christy Mahoney, for the hundreds of hours of moral support.

Tyler Jacobson, for being an amazing editor.

Michele De Giuli, for reminding me to eat and take breaks.

And most especially, Karen Darnell. Thank you Mom for everything you do.

There is no way to sufficiently express my gratitude.

TABLE OF CONTENTS

LIST OF TABLES

LIST OF FIGURES

1 INTRODUCTION

Astrochemistry, also known as molecular astrophysics, studies the "formation, destruction and excitation of molecules in astronomical environments and their influence on the structure, dynamics, and evolution of astronomical objects" (Dalgarno 2008). An interdisciplinary field, astrochemistry incorporates knowledge and practices not only from astronomy and chemistry, but also physics, math, biology, geochemistry, and informatics (van Dishoeck 2018). For nearly a century, scientists have been using optical absorption spectroscopy of atoms and molecules in diffuse clouds along the lines of sight to bright stars to discern the identity of those particles, and more importantly, what their presence signifies. Analysis of this data has been the key to answering questions about the temperatures, densities, gas masses, ionization rates, radiation fields, and other dynamics of regions of deep space.

The field of astronomy as a whole is interested in the development of the physical structures of the universe, from planets and asteroids to molecular clouds and nebulae. How these structures form and survive depends on complex interactions of chemical and physical processes. Chemical effects such as molecular cooling are an essential part of the massive dynamical processes studied by astrophysicists. At the same time, the energy necessary for chemical reactivity is provided by dynamical processes, such as the shocks created by high speed proto-stellar outflows, and radiative processes, such as photodissociation. Because physical and chemical phenomena are so deeply interdependent, it is imperative that the relevant scientists collaborate in order to understand them.

Matter that is at higher than average density can be used to trace and understand many of the most interesting astronomical phenomena (Fraser et al. 2002). Understanding how this matter interacts with light at a basic level allows for the observation of the movement of planets, stars, and galaxies. However, the interactions

of molecules and light also provide more precise tools for determining the physical conditions and processes observed within a region (van Dishoeck 2018), especially given the capacity of certain molecules to act as proxies for qualities that are more difficult to observe. Molecular tracers can include using CO as a proxy for hydrogen abundance (Herbst & van Dishoeck 2009), using the concentration of ammonia as a proxy for temperature (Ho & Townes 1983), and C_2 and HCN to indicate the density of gaseous regions (Butterfield et al. 2021).

With sufficient knowledge of astrochemistry, analysis of molecular tracers can also reveal events that preceded the current conditions of a region of study. Both current and previous physical conditions can be determined using models of the conditions under which molecules are created or destroyed, including which conditions cause molecules to enter the gas phase and which cause them to "freeze out." For example, many cosmic dust grains are composed of silicates that clump together, providing a surface for other molecules to freeze onto. If SiO is observed in the spectra, it tells us that there has been a shock that destroyed the dust grain, releasing SiO into the gas phase (Hogerheijde 2005). The physical conditions within that shock, such as speed and temperature, can then be determined by analyzing the prevalence of ionized atomic gases verses excited molecular species.

Molecular emission during physical events also provides methods for examining objects in space. Radiative cooling, thermal conduction, and electrion-ion energy equipartition (Draine 2010) all allow astronomers to determine physical conditions in a region. Take radiative cooling in low-density plasma, for example, which is caused by the collisional excitation of ions. Because radiative cooling limits gas pressure in collapsing clouds, it reduces the level of ionization, resulting in the weakened ability of the magnetic field to support the gas against collapse (Fraser et al. 2002).

Pre-stellar cores are formed when gas clouds collapse in this way, so detecting specific patterns of radiative cooling can help to isolate regions where stars will form.

Being able to accurately extrapolate conditions from molecular tracers is a crucial process in the search for life elsewhere in the universe. As astronomers investigate young stellar objects and regions of planetary formation for conditions where pre-biotic molecules could form, there is still much to be discovered about molecular behavior in space. More specifically, the differences in molecular behavior between the gas and solid phases are not thoroughly understood. Additional study is therefore needed on how molecules behave within solid-phase interstellar ices if we are to understand the origins of life.

The remainder of Chapter 1 is divided into three sections. Section 1.1 will review the process of spectroscopy, including both the molecular phenomena that result in spectra as well as the current tools used to collect those spectra. Section 1.2 will discuss key considerations when studying molecular reactions in deep space. These considerations include how molecules behave in the gas phase as well as how chemical reactivity differs between the surface and the bulk of cosmic ice grains. Finally, Section 1.3 will provide an overview of rate-based chemical modeling and radiative transfer modeling, as well as the limitations of those modeling processes when applied to interstellar objects.

1.1 Spectroscopy

Spectroscopy uses the properties of how matter interacts with electromagnetic radiation to study the physical and chemical properties of the phenomena being observed. Analyzing the light collected through telescopes and identifying which wavelengths have been emitted or absorbed allows for the identification of molecules present within the interstellar medium (ISM) as well as estimates of their abundances relative to the abundance of molecular hydrogen (Wakelam et al. 2010). Molecules

absorb and emit light from UV to millimeter wavelengths (van Dishoeck 2018) in accordance with the energy difference of their transitions. Molecular transitions can be electronic, vibrational, or rotational. The spectral lines that result from these transitions reveal temperature, density, energy, isotope ratios, and many more properties. This information allows chemists to determine what reactions are occurring.

1.1.1 Spectroscopic Transitions

Each type of transition is predominantly encountered in distinct ranges of the spectra. Electronic transitions are found within the optical and UV regions of the spectra (Fraser et al. 2002; van Dishoeck 2018). An electron jumps to a higher energy level when it absorbs a photon and decays to a lower energy level by emitting a photon. Based on the geometry between the energy source, the material being excited, and the observer, either absorption or emission lines will appear in the spectra. For hydrogen, the wavelength of these lines has been calculated for various transitions, as in the Balmer and Lyman series. For more complicated atoms and molecules however, the wavelengths of these transitions must be obtained experimentally. Several collections of these lines have been compiled, including the Splatalogue database for astronomical spectroscopy (Splatalogue 2012) and the Cologne Database for Molecular Spectroscopy (CDMS 2019).

Vibrational transitions, by contrast, are primarily found in the infrared region of spectra (Fraser et al. 2002; van Dishoeck 2018; Wakelam et al. 2010). The vibrational state of a molecule describes the oscillations of its bond lengths and bond angles. If these oscillations create or modify a dipole moment, vibrational transitions can be observed. A vibrational transition occurs when a photon is absorbed or emitted, changing the vibrational energy level of the bonds between the atoms in a molecule. Because vibrational transitions appear at infrared wavelengths, they allow for the

observation of regions with high optical extinctions such as the dust-obscured regions where stars are formed.

Rotational transitions are usually found in the radio or mm wavelength range (Fraser et al. 2002; van Dishoeck 2018; Wakelam et al. 2010). Only molecules with a permanent dipole have rotational transitions which occur as the molecule changes rotational state. Like electronic and vibrational energy levels, the "speed" of these rotations is quantized so that discrete photons are absorbed or emitted. Because these transitions occur at lower energies than electronic or vibrational transitions, they can be used to observe colder regions of space where molecules are in their electronic and vibrational ground states, like the interstellar medium (ISM).

The electronic, vibrational, and rotational states of a molecule interact with and influence the wavelengths of the transitions produced by the other types. For example, a molecule in an excited electronic state will have different bond lengths and a different dipole moment than the same molecule in the ground electronic state (Herzberg 1950). This will change the wavelengths observed in the vibrational and rotational transitions. Vibronic spectroscopy formalizes the interdependence of these transitional types.

While it is common to observe both vibrational and rotational transitions in the spectra, this is not the case when observing cold interstellar ices. In the solid phase, rotation is hindered while the molecules can still vibrate (Fraser et al. 2002). Consequently, analysis of these spectra can differentiate between gas-phase molecules and those that have frozen out onto dust grains.

1.1.2 Spectroscopic Analysis

Spectra collected via telescopes must be processed before analysis of spectral lines can be performed. The first step of this processing is the removal of the background. While the adjustments can be straightforward in cases where the background follows

a blackbody curve, the more chemically interesting regions such as dense molecular clouds more often exhibit overlapping blackbodies, thermal radiation, and radiative cooling around other objects in space that complicate the spectra.

Once the spectra has been isolated from the background, the idiosyncrasies of individual molecules must be taken into account. Atoms and molecules without a dipole moment, such as N_2, are difficult to detect because their dipole vibrational and rotational transitions are forbidden. Other molecules, such as $CH_3{}^+$, are so chemically reactive that they are not available in observable quantities. Classes of large, similar molecules, such as polycyclic aromatic hydrocarbons (PAHs), are also difficult to distinguish because their spectra are very similar to others in the same category (Fraser et al. 2002).

Astronomers have developed techniques for working around these difficulties. As mentioned above, some molecules can be used as tracers. Because CO is found in a known ratio to H_2, instead of attempting to detect H_2 through electronic and forbidden transitions, it is much simpler to detect CO with its permanent dipole moment (Fraser et al. 2002). Other tracers indicate the presence of physical conditions, such as the presence of silicates in the gas-phase indicating the occurrence of a shock releasing those molecules from dust grains (Hogerheijde 2005). With regards to composition, isotope analysis can help to determine concentration when the most abundant isotope in a region is optically thick (Guevara et al. 2020). Additionally, the absence or presence of specific gases in the spectra indicate temperature as the gases freeze out at varying temperatures (Lewis 1974).

1.1.3 Telescopes

Data collection via telescope is complicated by atmospheric interference. The molecules in Earth's atmosphere can produce significant complications in telescopic spectra. For example, ozone blocks UV light while water vapor and greenhouse gases

produce broad absorption lines in the IR. However, innovations in both ground-based and space telescopes have allowed astronomers to account for atmospheric interference in various ways.

Ground-based radio and IR telescopes are usually built at high-altitude sites where there is less atmosphere to provide interference. At these locations, the telescopes are frequently deployed not as a single instrument, but rather as an array, with several telescopes working together to increase the resolution of the observed spectra. Functioning as interferometers, these telescopic arrays are able to combine the signals of each individual telescope to improve the signal-to-noise ratio. Examples of these telescopes include those at Kitt Peak National Observatory (Saunders & Bruening 1968) and the Atacama Large Millimeter Array (ALMA) (Ishiguro 2001).

Space-based telescopes sidestep the issue of atmospheric absorption entirely. Following the launch of the famous Hubble Space Telescope, which observes primarily visible wavelengths (Jakobsen & Laurance 1989), newer space telescopes have been able to capture a broader range of the electromagnetic spectrum, including mid- and far-infrared wavelengths. Among these telescopes are the Infrared Space Observatory (ISO) (Kessler et al. 1996), the Herschel Space Observatory (Tofani & Natale 2003), and the Spitzer Space Telescope (Werner et al. 2004), which have all proved to be invaluable resources for observing the molecular universe (Wakelam et al. 2010).

The James Webb Space Telescope is the newest of these space telescopes (Gardner et al. 2006). While the primary mission of the JWST is to observe high-redshift galaxies, the high resolution spectra collected by the JWST are a great resource for astrochemists interested in the near- to mid-IR range. Heat creates noise in IR spectra, and thus the Sun, the Earth, and the Moon all radiate IR interference. However, because the JWST has been placed into orbit around the L2 Lagrange point, the telescope's sun shields can block the background from these sources. As a

result, the JWST will have a significantly greater capacity to detect the vibrational modes of solid-phase molecules in interstellar ices, which currently remain broadly inaccessible to astrochemists (Lemonick 2021).

A third class of telescopes attempts to combine the best characteristics of both ground-based and space telescopes. The Stratospheric Observatory for Infrared Astronomy (SOFIA) is a modified Boeing 747 that collects data during carefully planned flight paths through the stratosphere (Erickson 1992). At this height, SOFIA is able to collect spectra from IR regions that are normally absorbed by the atmosphere before they can reach ground-based telescopes, just like a space telescope. However, as an airplane, SOFIA can also return to the ground for maintenance, upgrades, and the implementation of new technologies.

With an ever-increasing selection of available telescopes, astronomers are able to access parts of the electromagnetic spectrum that had previously been blocked by atmospheric interference. This clearer view of the cosmos allows for the more precise identification of the spectral signatures of a much greater number of interstellar molecules, which then allows for the identification of a proportionately greater number of chemical reactions occurring in space.

1.2 Reactions in Space

Through the use of the telescopes discussed above, astrochemists have been able to identify a great number of molecules in space. As of September 2021, it was reported that over 240 molecular species, comprised of 19 different elements, had been detected and identified within interstellar and circumstellar mediums (McGuire 2022). Most of these molecular species are electrically neutral, being either unsaturated molecules or free radicals (Wakelam et al. 2010).

Within molecular clouds, these molecular species are found either in the gas phase or within the ice mantle of a dust grain. The reactions and physio-chemical processes

that produce and destroy these molecules are driven by various sources of energy, though the consequences of those processes may vary depending on whether they occur in the gas phase, at the gas-solid interface, or within the solid bulk of an ice mantle. These energy sources are summarized in Figure 1.

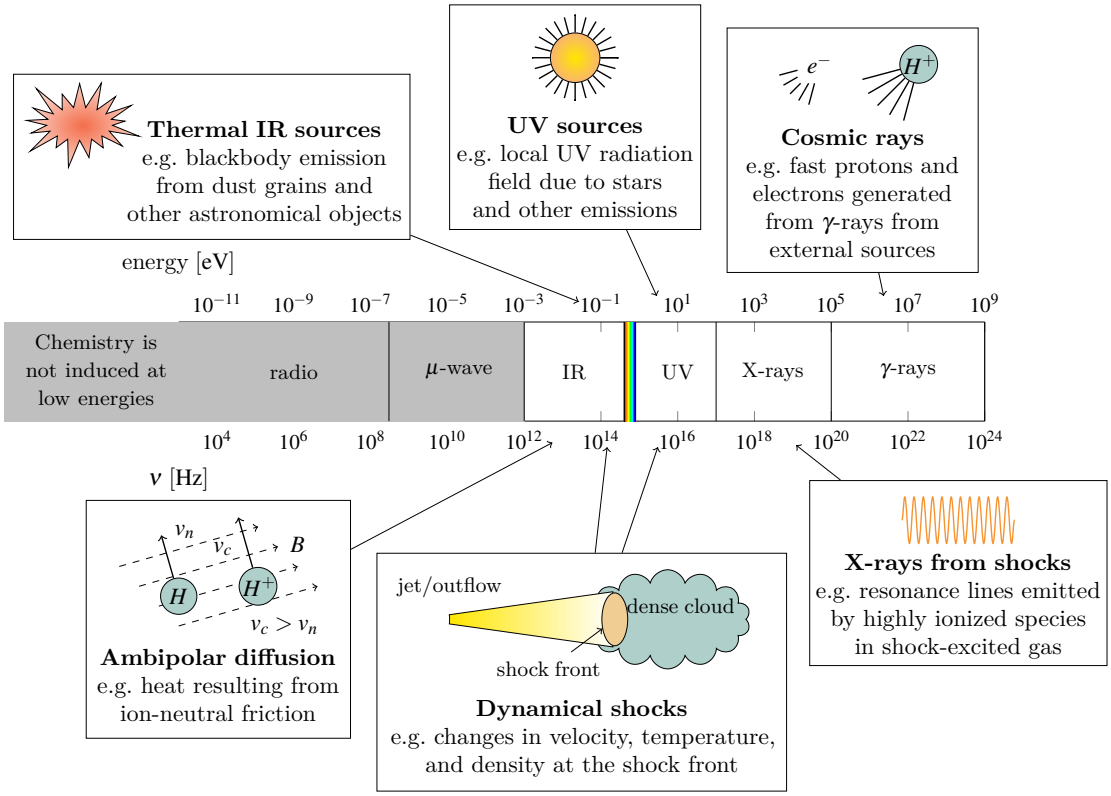

Fig. 1: Energy Sources in Space Shown are the sources of energy that drive chemical reactivity in interstellar and circumstellar regions of space. Adapted from Figure 2 in Fraser et al. (2002)

Thermal energy at the edges of a molecular cloud or in a diffuse medium is usually supplied by an ambient UV photon field called the Interstellar Radiation Field (ISRF) or by nearby hot stars. The ISRF heats surrounding gas and dust, providing energy for reactions. The resulting blackbody emissions of these dust grains are a thermal IR source, causing previously formed ices to evaporate (Fraser et al. 2002). However, within the cold dense cores of molecular clouds, the ISRF is extinguished in the outermost layers. This means the UV photon flux from the ISRF is negligible in the

interior of the cloud and temperatures drop as low as 7 K (Evans et al. 2001). The energy that drives reactivity must come from other sources, including cosmic rays, γ-rays, and the internal UV photons they produce upon interacting with molecular hydrogen (Prasad & Tarafdar 1983). Ion-neutral reactions dominate the gas-phase chemistry at these low temperatures (Fraser et al. 2002; Herbst & Klemperer 1973).

1.2.1 Gas-Phase Chemistry

Most molecules in the ISM are encountered in the gas phase where atoms and molecules are mobile and energetic. All reactions in the cold ISM are exothermic and either involve tunneling or having negligible activation energy barriers. The chemistry relevant to this research is triggered by processes that occur when a molecule or atom absorbs a photon with sufficient energy. This can result in the excitement of an electron to a higher energy level (photoexcitation) or the ionization of the species (photoionization). Photodissociation occurs when a molecule is excited to a higher energy repulsive state via photoexcitation that then then rapidly dissociates before it can decay back to a lower energy level.

Gas-phase chemistry also exhibits collisional reactions, which occur when two or more molecules/atoms/ions collide at the right orientation. Collisional reactions can be subdivided into ion-neutral reactions, neutral-neutral reactions, and charge transfer reactions. See Figure 2 for a list of chemical reactions that occur in space.

Recombination reactions occur when a negatively charged species reacts with a neutral or positively charged species. In the gas phase, when a molecular species is involved in such a reaction, the energy released is used to cleave a chemical bond through a process known as dissociative recombination. In atomic species, however, the energy is instead emitted as a photon in a process known as radiative recombination or association. This process is called self-quenching, and it is a mechanism for radiative cooling (Herbst & Millar 2008).

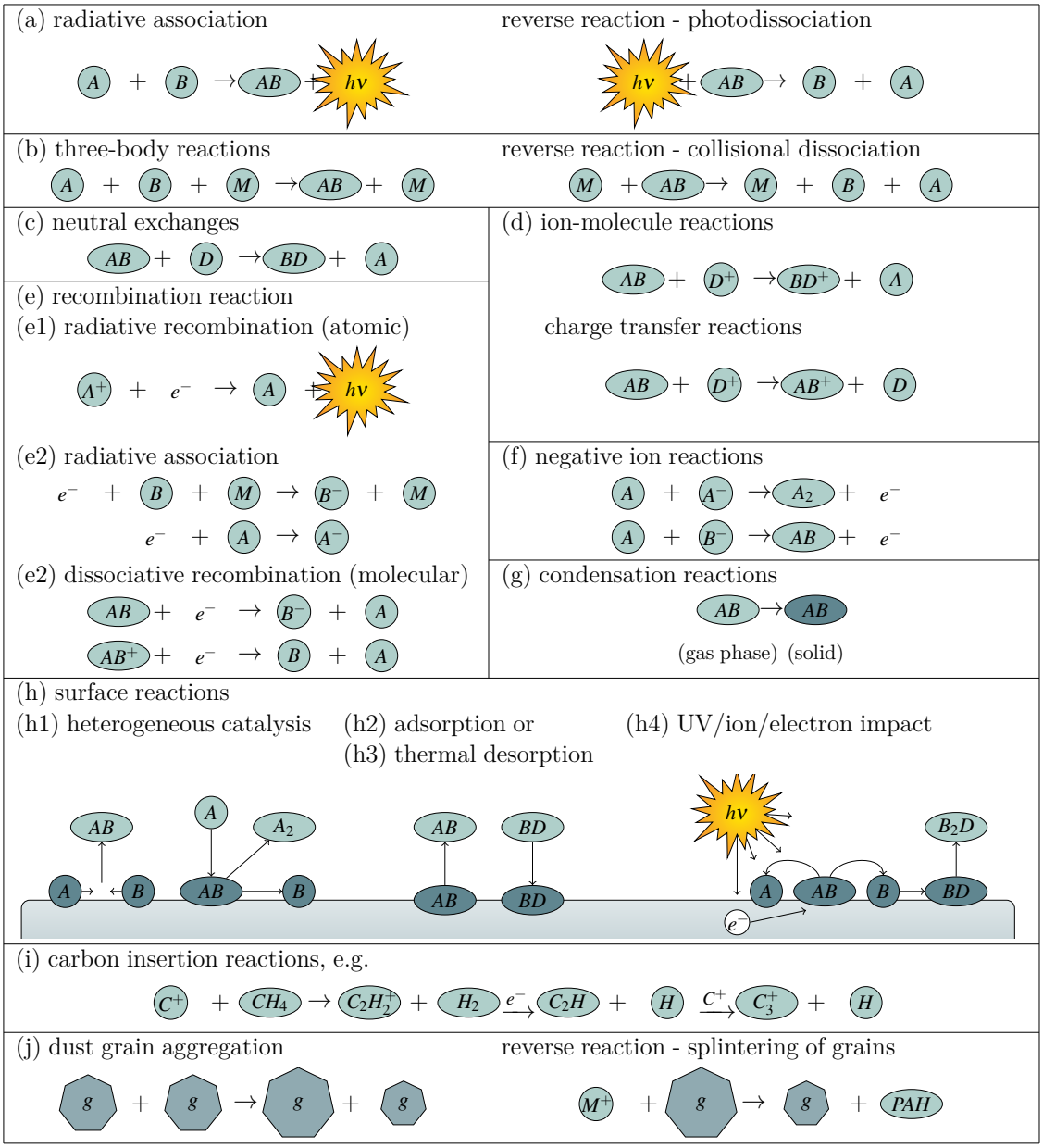

Fig. 2: Interstellar Chemical Reactions Adapted from Figure 1 in Fraser et al. (2002)

Depletion or condensation reactions occur when a molecule transitions from the gas phase to the solid phase by "freezing out" onto a dust grain or ice mantle. In principle, this can help determine the age of a molecular cloud (ex. by $\sim 10^5$ yr CO is primarily on the grain (Boogert et al. 2015) but in practice it is too uncertain.

1.2.2 Grain Chemistry

The silicate cores of an interstellar dust grain are formed in the outflows of dying stars. Volatile molecules then condense onto the core via depletion, creating monolayers that form the ice mantle. The chemical reactivity of the mantle is considered in two parts: the surface, which is comprised of the top four monolayers, and the underlying bulk. This structure is illustrated in Figure 3.

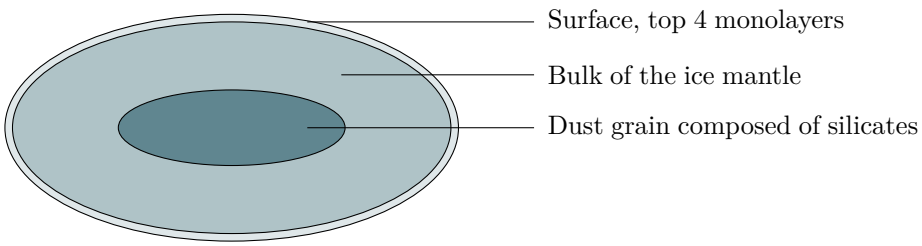

Fig. 3: Layers of an Interstellar Dust Grain

1.2.2.1 Surface Chemistry

The most important reactions on the surface of interstellar ices are heterogeneous catalysis, thermal desorption, and impact by radiation. Heterogeneous catalysis occurs when the phase of the reactants is different from the phase of the catalyst. For interstellar ices, gas-phase reactants called adsorbates are adsorbed onto the surface of a dust grain, where they react with the surface before undergoing desorption. Typically, the adsorbates "stick" to the surface of the grain via van der Waals forces in a process called physisorption. However, in high-temperature regions, adsorbates can also be attached to the bare grain surface by strong chemical bonds in a process called chemisorption (Acharyya et al. 2020).

Molecular collisions on grain surfaces occur through one of two mechanisms (Acharyya et al. 2020). In the Langmuir-Hinshelwod mechanism (Figure 4a), reactants diffuse across the surface and react upon collision. In the Eley-Rideal mechanism (Figure 4b), an adsorbate is held stationary on the surface, where it reacts

with a colliding gas species. On the surface of ices in dark, dense molecular clouds, the diffusive Langmuir-Hinshelwod mechanism is more common. As more species are adsorbed onto the grain, they begin to cover the grain surface, including the previously adsorbed species and the products of their reactions. Over time, this forms the ice mantle.

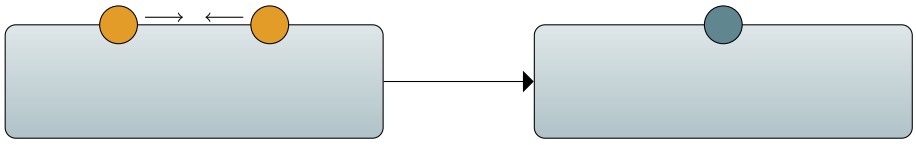

(a) Langmuir-Hinshelwod mechanism Reactants diffuse across the surface and react upon collision.

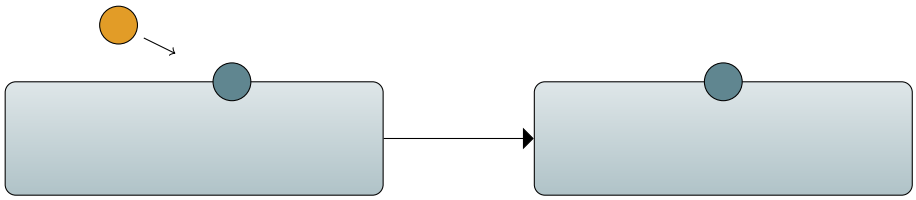

(b) Eley-Rideal mechanism An adsorbate is held stationary on the surface, where it reacts with a colliding gas species.

Fig. 4: Surface Reaction Mechanisms

If temperatures rise sufficiently, molecular species within the ice mantle may begin to diffuse and desorb throughout the grain. Thermal desorption energies govern when a species will be present on the surface of the grain and thus available to react. When the thermal energy reaches the desorption energy for a particular species, there are three possible outcomes. First, the molecular species can decompose to form either gas phase products or other surface species (Figure 5a). Alternatively, the species can react with another species on the dust grain to form a surface compound, or it may diffuse into the bulk of the ice mantle (Figure 5b). Finally, it is possible that the species can desorb from the surface entirely and return to the gas phase (Figure 5c). These processes are illustrated in Figure 5.

While the desorption energies of pure ices on various substrates have mostly been determined, the desorption energy of any one species within the mixed layers of a dust

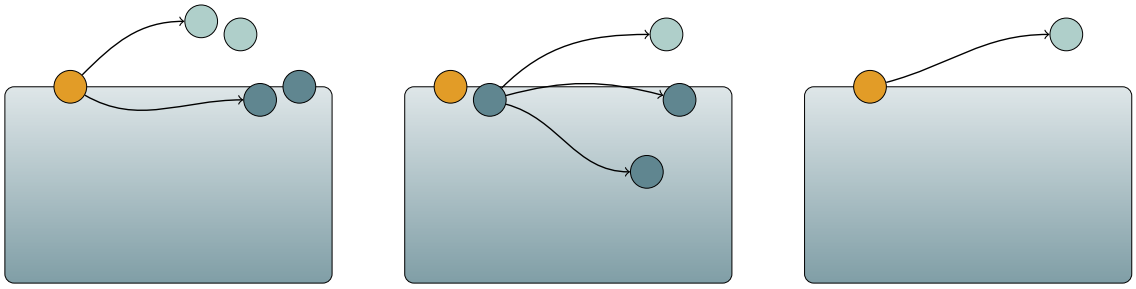

(a) The species decomposes to form either gas phase products or other surface species.

(b) The species reacts with another species on the dust grain to form a compound that then desorbes, remains on the surface, or diffuses into the bulk of the ice mantle.

(c) The species desorbs from the surface and returns to the gas phase.

Fig. 5: Desorption processes A surface species can reach its desorption energy through transfer of thermal energy (pyrolysis), or due to collision from high energy protons (radiolysis) and photons (photolysis). The energetic surface species (depicted in orange) is then either quenched or undergoes one of three processes.

grain is dependent on the surrounding material (Wakelam et al. 2010). As more molecular species are introduced into the ice, the desorption process becomes more complex because the surrounding material can change a molecule's desorption energy, and the dominant mantle species can prevent the other species from desorbing. For example, CO and CO_2 can become trapped in a predominately water ice mantle due to the much higher desorption temperature of water (Collings et al. 2004). However, over a long time scale, parameters including surface temperature, ice composition, and mixing ratio may cause the dominant species in the mantle to slowly separate. This segregation of species allows trapped species to escape (Öberg et al. 2009).

Aside from thermal desorption, surface species may escape a grain below their desorption energies if affected by cosmic-ray spot heating, chemical desorption, or grain-grain collisions (Hogerheijde 2005). Cosmic-ray spot heating occurs when a cosmic ray travels through a grain, heating a cylindrical region where the material may then desorb (Hasegawa & Herbst 1993). Chemical desorption is a disputed mechanism that occurs when an excited molecule vibrates off the grain before the

grain absorbs the energy (Garrod & Herbst 2006). In grain-grain collisions, the energy required for desorption is provided by the energy of the collision itself; however, this process has not yet been studied in detail. By contrast, collisions between grains and radiated particles have been studied extensively under the name of radiation chemistry.

Radiation chemistry, also known as photochemistry, is the dominant chemistry occurring in cosmic ices in dark, dense molecular clouds (Arumainayagam et al. 2019; Mullikin et al. 2021). Cosmic rays, as well as the UV photons that result when cosmic rays interact with gas-phase hydrogen, produce electronically excited (suprathermal) species and secondary electrons. In the gas phase, suprathermal species will dissociate before reacting with anything, but in the solid phase, species can quickly react with their neighbors before dissociating. This proximity allows endothermic reactions to occur. Some fraction of the suprathermal species will result in photodesorption.

1.2.2.2 Bulk Chemistry

The bulk of an ice grain is comprised of the material below the top four monolayers of the mantle. It is assumed that thermal processes do not occur in the bulk due to the shielding provided by the outer layers, which means chemical reactivity in the bulk relies on other processes. The traditional understanding of grain chemistry has held that UV photons can cause photodissociation that results in the formation of bulk products that only recombine into new molecular species when the ice mantle begins to warm up (Acharyya et al. 2020; Garrod et al. 2008; Herbst & van Dishoeck 2009; Theulé et al. 2013). However, this approach proves difficult to model because the model has to account not only for how each species will diffuse through the ice, but also how the desorption energy of each entrapped species is changed by the ice that shields it. Additionally, such models cannot account for the behavior of ices in cold dark cores where it remains too cold for thermal diffusion.

Even without the activity of thermal processes, the bulk of the ice is not chemically inert. While the outer monolayers do shield from thermal energy, they do not block cosmic rays and other energetic particles, so chemistry driven by photoprocesses can still occur. Photodissociation is the primary mechanism by which the molecules in interstellar ices are broken down into components that often recombine into new molecular species through thermal processes. However, as research has started to explore chemical reactions that occur before the ice heats up, it has become clear that further study on non-thermal reaction pathways is needed.

1.3 Modeling

Astronomical data can be modeled in a number of ways depending on the data set. Astrochemical research uses chemical modeling to understand and predict characteristics of chemical abundances in space. However, research involving telescopic spectra benefits as well from radiative transfer modeling, which considers how matter interacts with light to produce specific patterns of spectral lines.

1.3.1 Rate Based Chemical Modeling

Chemical models are used to understand how interstellar molecules are created within observed abundances. Current chemical models account for upwards of 400 chemical species linked by over 4000 reactions (Fraser et al. 2002; Wakelam et al. 2010). The reaction data incorporated into a model must describe the rate equations, rate coefficients, reactants, and products of each elementary process, which rapidly increases complexity. The molecular abundances predicted by the model are then compared with those derived from spectroscopic observations or those produced in laboratory experiments. The level of agreement between these observations and models becomes a measure of the success and efficacy of the model (Wakelam et al. 2010).

The reaction rate coefficients (also known as rate constants) used in these models have typically been derived experimentally. However, rate constants are frequently temperature dependent, and experiments on Earth are rarely conducted at temperatures equivalent to those in space. The rate constants used in models are typically extrapolated from experimental rate constants at higher temperatures or mathematically estimated from proposed reaction mechanisms. For example, the rate of a first-order reaction such as

$$A \rightarrow \text{products} \tag{1}$$

can often be described by the Arrhenius equation

$$k(T) = A \exp\left(-\frac{E_a}{RT}\right) \tag{2}$$

where A is a temperature independent constant and E_a is the activation energy.

In general, the concentration of a species is not determined by a single reaction. Instead, a rate law for the species must be derived by the sum of all of the formation and destruction pathways of that species. For example, in the small network modeled below

$$A \underset{k_{-1}}{\overset{k_1}{\rightleftharpoons}} B \tag{3}$$

$$A \underset{k_{-2}}{\overset{k_2}{\rightleftharpoons}} C \tag{4}$$

the differential rate equation for A would be given by

$$\text{Rate of change in } A = \text{Destruction of } A + \text{Formation of } A \tag{5}$$

$$\frac{d[A]}{dt} = -(k_1 + k_2)[A] + k_{-1}[B] + k_{-2}[C] \tag{6}$$

In rate-based modeling a differential rate equation is created for each species in the network, and the system of equations is then solved.

Steady-state modeling assumes that the time derivative of all concentrations is set to zero, $\frac{d[A]}{dt} = 0$ (Wakelam et al. 2010), in other words the rate of formation of each molecule is equal to the rate of destruction of that molecule. Because different species reach their steady-state concentrations at different times, the steady-state values of the species that approach steady state more quickly can be used to constrain the differential equations of species that approach steady-state more slowly (Herbst & Klemperer 1973). While convenient for researchers calculating by hand, steady-state modeling demands certain constraints. For example, the time needed to reach chemical equilibrium must be shorter than the lifetime of the environment being modeled, or else the environment will not actually be in a steady state. Steady-state modeling does not give any information on how the system arrived at steady state. The increase in computational power of modern computers has allowed time-dependent modeling to replace steady-state modeling as the standard modeling technique.

Time-dependent modeling allows for molecular abundances to be predicted as a function of time given a few key assumptions about starting conditions, such as the temperature, the chemical species present and their relative abundances, and the physical state of the species (Wakelam et al. 2010). While these models are more complex, they allow for modeling of tumultuous regions of space in which species will never reach the steady state before environmental conditions change. The primary challenge for designers of this type of model is determining which time step is most relevant. For such a model to be successful, it must account for not only the physical and chemical processes that impact elemental composition (such as deposition, evaporation, and chemical reactions), but also the physical and chemical parameters

that govern the rates of reaction. These parameters include factors such as temperature, density, ionization rate, desorption energies, and activation energies.

1.3.2 Radiative Transfer Modeling

Radiative transfer modeling is the process by which the physical and chemical properties of an object are used to predict the spectra that the object will produce. The observed lines are determined by the electronic, vibrational, and rotational modes of molecular species, each of which registers as a unique pattern of spectral lines. When a radiative transfer model is applied to the results of a chemical model, synthetic spectra are created in accordance with the assumed species present, their concentrations, and the temperature of the region. These synthetic spectra thus allow for evaluation of the accuracy of the original chemical model.

Radiative transfer modeling makes use of several equations to cross-infer relationships between the conditions of a region and the qualities of the molecular species present there. The Boltzman equation (Equation 7) quantifies the number of atoms in different energy states based on the temperature of a region:

$$\frac{N_b}{N_a} = \frac{g_b}{g_a} e^{-(E_a - E_b)/kT} \tag{7}$$

where $\frac{N_b}{N_a}$ is the ratio of atoms in energy state b to energy state a, and g_b and g_a are the number of degenerate states of energy E_b and E_a respectively.

The Saha equation (Equation 8) describes the ratio of atoms different ionization states:

$$\frac{N_{i+1}}{N_i} = \frac{2kTZ_{i+1}}{P_e Z_i} \left(\frac{2\pi m_e kT}{h^2} \right)^{3/2} e^{-\chi_i/kT} \tag{8}$$

where $\frac{N_{i+1}}{N_i}$ is the ratio of atoms ionization state $i+1$ to ionization state i, Z_i and Z_{i+1} are the partition functions for the atom in its initial and final stages of ionization, and χ_i is the ionization energy.

Radiative transfer modeling is concerned with interpreting the dimensions of the lines that appear in spectra. While line intensity is determined by the the number of atoms in each energy or ionization state, determining the width of a spectral line is a more complicated process due to various broadening effects.

Natural broadening, sometimes called lifetime broadening, is due to quantum mechanical effects, i.e. that it is impossible to exactly determine the energy distribution of the system over a changing time ($\Delta E \Delta t \sim \hbar$). This determines the natural shape of the line. The Lorentz (or natural) profile is given by equation 9,

$$\phi(\nu) = \frac{\gamma/4\pi^2}{(\nu - \nu_0)^2 + (\gamma/4\pi)^2} \tag{9}$$

where γ is the rate of spontaneous decay of the atomic state, and ν_0 is the rest-frame frequency (Rybicki & Lightman 2008). The Lorentz profile of a molecular species must be modified to account for factors such as collisional broadening, which occurs when atoms collide while emitting.

Doppler broadening, which modifies the natural profile of the line, is caused by thermal and physical motion of the molecular species. Each atom has a Doppler shift, which in net broaden the spectral line. The effective Doppler width is given by

$$\Delta\nu_D = \frac{\nu_0}{c}\sqrt{\frac{2kT}{m_a} + \xi^2} \tag{10}$$

where ν_0 is the rest-frame frequency and ξ^2 is the root mean-square of the turbulent velocities (Rybicki & Lightman 2008). By combining these principles, a synthetic spectrum can be created from the results of a chemical network model, which can then be compared with observed spectra.

1.3.3 Modeling limitations

While chemical modeling has allowed for a great number of astronomical discoveries, it is important to also recognize the limitations of the modeling process.

Models make use of astrochemical databases, many of which remain incomplete and are only updated on a 'best effort' basis due to the sheer amount of data that has yet to be compiled (van Dishoeck 2018). Additionally, the energy sources of a region must all be considered when selecting a reaction network to model, but many of these sources are still being identified in the regions of space least accessible to observation from Earth. One crucial hindrance to astrochemical modeling is that there is currently no irradiated ice model that accounts for ion-neutral reactivity. The present research seeks to provide one such model in order to move towards greater understanding of the behavior of interstellar molecules found in the solid state.

2 BACKGROUND/LIT REVIEW

2.1 General Background

In 1973, Herbst and Klemperer were the first to demonstrate that the chemistry of dense molecular clouds is driven by cosmic rays that initiate networks of ion-molecule reactions. Their steady-state quantitative model relied almost exclusively on gas-phase chemistry (Herbst & Klemperer 1973). Within the gas phase, the molecular abundances they observed were relatively stable with respect to total gaseous density and ionization rate because of balanced formation and destruction rates. Because molecular densities in the gas phase are too low for efficient three-body reactions, Herbst and Klemperer's model only included binary collisions. Additionally, only exothermic reactions with a negligible activation energy barrier occur due to the low kinetic temperature within dense clouds. This means that the major pathways for polyatomic molecule synthesis must be exothermic ion-molecule reactions. Within these dense clouds, cosmic ray bombardment results in the formation of positive ions, from which McCray & Dalgarno (1972) extrapolated that positive ion-neutral reactions were more prevalent and thus more important to gas-phase chemistry models compared to negative ion reactions .

After Herbst and Klemperer had explored gas-phase ion-molecule reactions within low temperature dense interstellar clouds, further research began to find that gas-phase models alone cannot fully describe the chemical complexity implied by the detection of increasingly complex organic molecules (Hasegawa et al. 1992; Wakelam et al. 2010). Consequently, further models began to explore the chemistry on low temperature grain surfaces (Allen & Robinson 1977; Pickles & Williams 1977; Tielens & Hagen 1982). However, while gas-grain models offered more complex accounts of interstellar molecular formation, such models are limited because they rely on poorly constrained hypotheses about the energy barriers of surface diffusion and surface

reactions of interstellar dust grains (Wakelam et al. 2010). In order to accurately describe this chemical complexity, models need to account for not only surface and bulk processes triggered by thermal processing, but also those caused by particle bombardment and photon irradiation (Gibb et al. 2004). Additionally, a more nuanced understanding of how each of these processes differs within the bulk compared to the surface is still needed.

While it is assumed that thermal desorption is the primary pathway through which molecules are formed from the bulk material of the ice mantle, there are significant challenges to modeling this type of chemistry. As discussed in Section 1.2.2.1, each molecular species has its own desorption energy which can also be changed by the composition of the surrounding material. Consequently, models must account for every context in which a molecular species may be found within the grain, which means such models are incredibly difficult to scale beyond pure ices or simple mixtures.

Desorption energies must be obtained experimentally or calculated using quantum chemistry as in the work of Cuppen et al. (2018); Penteado et al. (2017) However, these methods are labor intensive and difficult to scale even with the increase in processing power provided by modern computers. In addition, it is not well understood how an ion's movement through the ice mantle as it warms differs from the movement of a neutral species. This means that ions have been excluded from grain models despite the importance of ion-neutral chemistry in the gas phase. Fortunately, these challenges are specific to thermal chemistry.

Experiments have demonstrated that reactions in irradiated ices proceed more rapidly than can be explained with thermal-diffusive mechanisms. Gerakines et al. (1996) showed that UV photolysis of pure ices could produce new species, including free radicals and some large organic species. Baragiola et al. (1999) as well as Raut

et al. (2011) were able to synthesize ozone by irradiating thin cold films of oxygen and oxygen-water mixtures. Both of these experiments demonstrated that irradiated interstellar ices undergo chemical reactions that are not dependent on thermal desorption mechanisms.This implies that reactions proceed via a non-diffusive mechanism.

Understanding how interstellar chemistry functions in the absence of thermal diffusion is crucial for the study of cold dark cores such as the Taurus Molecular Cloud 1 (TMC-1). In these regions, light is attenuated by the surrounding material and it is too cold for thermal diffusive chemistry to occur. By contrast, cosmic rays are not attenuated by high numbers of collisions, so they can interact with the matter in cold dark cores. These highly energetic particles permeate interstellar space and have significant effects on the physical and chemical properties of the matter they interact with (Shingledecker & Herbst 2018). Aside from ionizing gas-phase molecules leading to ion-neutral chemistry, cosmic rays can desorb grain-surface species non-thermally and generate UV photons upon interacting with gas-phase hydrogen. These photons then drive photoionization and photodissociation within the optically thin ice mantle (Mullikin et al. 2021), which in turn drives internal solid-phase bulk chemistry. Modeling non-thermal radiation chemistry within the bulk of the ice in this way bypasses the factors that render thermal desorption modeling ineffective within cold dark cores.

Nevertheless, current astrochemical models have not yet developed a thorough understanding of solid-phase radiation chemistry because the underlying microscopic processes are complex, and also because of a lack of radiochemical data for many molecular species. The cosmic ices within these cold dark cores are continuously irradiated by cosmic rays and the UV photons they produce. This radiation has significant physical and chemical effects on the ice, including the formation of ions.

Therefore, models of interstellar ice that do not account for the behavior of ions produced by ionizing radiation will fall significantly short of physical realism.

2.2 Project Specific Background

Shingledecker & Herbst (2018) developed a formalism focused on solid phase chemistry that estimates the rate coefficients of radiolysis decomposition pathways such that radiation chemistry can be included within a typical rate equation astrochemical model.

Starting with the assumption that the "essential astrochemically relevant features of irradiation chemistry are (a) the ionization and excitation of target species, (b) the destruction of the target species via charge neutralization and excitative dissociation, and (c) the formation of radiolysis products, including electronically excited suprathermal species" he concluded that there are four basic decomposition pathways that occur after bombardment by an energetic particle given by photo processes (P1)–(P4) (Shingledecker & Herbst 2018).

$$A \rightsquigarrow A^+ + e^-, \tag{P1}$$

$$A \rightsquigarrow A^+ + e^- \rightarrow A^* \rightarrow B^* + C^*, \tag{P2}$$

$$A \rightsquigarrow A^* \rightarrow B + C, \tag{P3}$$

$$A \rightsquigarrow A^* \tag{P4}$$

Here the star superscript indicates an electronically excited, or suprathermal, species. An advantage of explicitly including reactions (P1)–(P4) in the model is that the reverse reactions can be included in the general network of reactions to be accounted for separately. This allows us to focus on only the photolysis pathways of A, simplifying the modeling process. It is assumed that suprathermal species rapidly react, dissociate, or are quenched by the surrounding solid once they are formed

(Shingledecker & Herbst 2018). If one of the reactants is a suprathermal species, the reaction will have a negligible reaction barrier even if the ground state of that reaction would have a significant energy barrier. Experiments (Abplanalp et al. 2019; Kleimeier et al. 2021) have shown that these suprathermal species are important in driving non-equilibrium low-temperature solid-phase chemistry.

To calibrate this model, Shingledecker et al. (2019) recreated the results of proton irradiation of pure water and oxygen ice experiments done by Baragiola et al. (1999) and Gomis et al. (2004). By comparing the results of three scenarios, they determined that the scenario that best matched the experiments named above was the one in which reactions proceeded non-diffusively with neighboring species in the ice as shown in Figure 6.

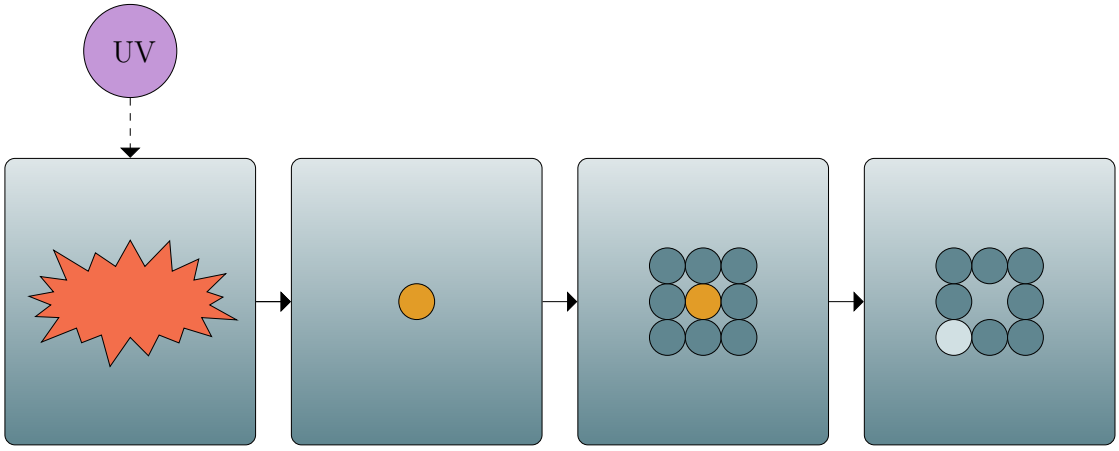

Fig. 6: Non-diffusive Mechanism A high energy proton or a UV photon bombards the ice mantle creating a reactive species within the bulk, depicted in orange. The reactive species is surrounded by other species in the ice mantle that are available to react. As the reactive species vibrates it can form an activated complex with one of its neighbors and thus a reaction can occur.

The model was then extended to account for non-thermal bulk chemistry driven by UV photons created by the interaction between cosmic rays and gas-phase hydrogen. In the ISM, fluxes are low enough that the number of photons that reach the inner monolayers of a dust grain is still uncertain; however, in cold dark clouds fluxes are high enough that the entirety of the ice is irradiated by UV photons. These

photons irradiate the optically thin ices to drive non-thermal chemistry within the bulk of the ice. Mullikin et al. (2021) explicitly considered photoionization and photoexcitation processes and used the expanded model to recreate the results of Gerakines et al. (1996) and Raut et al. (2011). Mullikin et al. (2021) were able to, for the first time, successfully reproduce the results of a photochemical experiment in an astrochemical model with very good agreement. This study validated the utility of the present study's approach to photochemical processes and of the general method of constraining chemical networks based on the direct simulation of experimental work.

The goal of the present research is to expand on Mullikin's model of non-thermal bulk chemistry to include ion-neutral chemistry. We contend that it is possible to add ion-neutral chemistry into our model because thermal diffusion does not occur within the bulk of ices in cold, dark regions, which means our model does not need to account for how ions diffuse through the bulk. Additionally, we are modeling the bulk chemistry of optically thin ices to remove uncertainties caused by desorption on the surface. We know from gas-phase modeling that ion-neutral reactions are efficient pathways for molecular formation, yet they have not been included in previous grain models. By adding ion-neutral chemistry to the network, we will be able to determine how important ions are to non-thermal bulk chemistry and determine the impact of the exclusion of ion-neutral chemistry from models of molecular behavior in interstellar ices.

With the updated network, we will produce a model that can reproduce the experimental results obtained by Gerakines et al. (1996) which studied the photolysis products resulting from the irradiation of various ices. By restricting our model to pure oxygen ice, we ensure that our simulated system is well-constrained, allowing for comparison with the results obtained by Mullikin et al. (2021). The significance of the ion-neutral reactions in the formation and destruction pathways of ozone will

demonstrate the importance of ion-neutral reactions to non-thermal bulk chemistry. If the ion-neutral reactions are significant pathways to the formation and destruction of ozone under interstellar conditions, as simulated in the laboratory studies, then the traditional exclusion of these reactions will be proven to be erroneous.

3 METHODS

In order to understand ionic reactivity in interstellar ices, we incorporated data for ionic behavior into an existing model of ice chemistry. Section 3.1 describes the theoretical framework of the model and network. Section 3.2 describes technical details of the code and modeling parameters. Section 3.3 describes the model outputs and how the data was prepared for analysis.

3.1 Theory

Cosmic rays can interact with gas-phase hydrogen in cold dense molecular clouds to produce UV photons in regions where light would not normally penetrate. We assume that the interaction between these UV photons and some target species A within the ice mantle results in one of four outcomes:

$$A \rightsquigarrow A^+ + e^-, \tag{P1}$$

$$A \rightsquigarrow A^+ + e^- \rightarrow A^* \rightarrow B^* + C^*, \tag{P2}$$

$$A \rightsquigarrow A^* \rightarrow B + C, \tag{P3}$$

$$A \rightsquigarrow A^* \tag{P4}$$

These processes proceed at a rate determined by the standard formula for photolysis rates (Shingledecker et al. 2019) given by

$$k_{photo} = \int \sigma(\lambda) I(\lambda) d\lambda \tag{11}$$

where $\sigma(\lambda)$ and $I(\lambda)$ are wavelength dependent cross-section and photon flux, respectively. This equation can also be written such that the rate is equivalent to the average cross section of the species ($\bar{\sigma}$) multiplied by the integrated flux (Φ).

$$k_{photo} = \frac{\int \sigma(\lambda) I(\lambda) d\lambda}{\int I(\lambda) d\lambda} \int I(\lambda) d\lambda = \bar{\sigma}\Phi \tag{12}$$

Applying this rate to photoprocesses (P1)–(P4) we get

$$k_{P1} = P_e \bar{\sigma}_{ion} \Phi \delta, \tag{13}$$

$$k_{P2} = (1 - P_e) \bar{\sigma}_{ion} \Phi \delta, \tag{14}$$

$$k_{P3} = P_{dis} \bar{\sigma}_{exc} \Phi \delta, \tag{15}$$

$$k_{P4} = (1 - P_{dis}) \bar{\sigma}_{exc} \Phi \delta, \tag{16}$$

where P_e is the probability that the secondary electron produced in an ionization will escape, P_{dis} is the probability of dissociation, $\bar{\sigma}_{exc}$ and $\bar{\sigma}_{ion}$ are the average excitation and ionization cross sections obtained from the Leiden Photochemistry Database (Heays et al. 2017), and δ is a delta fitting factor. The delta fitting factor compensates for unknown influences on the rate, whether those be bad assumptions within the code, poor constraints of the network and associated branching functions, or factors that have not yet been identified or defined, such as reactivity due to secondary electrons.

Within the bulk, species have the opportunity to react with their neighbors upon each vibration. These reactions occur at the rate calculated by the process below (Shingledecker et al. 2019),

$$k_{fast} = f_{br} \left[\frac{\nu_0^A + \nu_0^B}{n_{bulk}} \right] \exp\left(-\frac{E_{act}^{AB}}{T_{ice}} \right) \tag{17}$$

where ν_0^A and ν_0^B are the vibrational frequencies of reactants A and B, E_{act}^{AB} is the activation energy of the reaction given in Kelvin, n_{bulk} is the volume density of the bulk of the ice which acts as a dilution factor, and f_{br}, or branching fraction, is the probability that the reaction will proceed in preference to reactions with competing product channels.

Within the bulk, suprathermal species (A^*) are assumed to either rapidly react with a neighboring species or to be quenched by the surrounding material. The reactions involving a suprathermal species or an ionic species are assumed to proceed without barriers. $\nu_0^{neutral}$ is set to $1 \times 10^{15}\,\mathrm{s}^{-1}$ and ν_0^{ion} is an adjustable parameter in the code, which in this work was set to $700\,\mathrm{s}^{-1}$. Branching fractions were assumed to be split equally between competing reactions unless sources included branching fractions.

While Eq. 17 sums the vibrational frequencies of the reactants together, within our code the model is programmed to instead only use one value, depending on whether an ion is present within the reaction. This means that for neutral-neutral reactions the rate constant is of the order $10^{-8}\,\mathrm{cm}^3/\mathrm{s}$ and both ion-neutral and ion-ion reactions have rate constants of the order $10^{-20}\,\mathrm{cm}^3/\mathrm{s}$. This was done because during initial testing, the modeled ion-neutral reactions proceeded far too quickly compared to the experimental data, so we needed to introduce an adjustable factor in the rate in order to slow down these reactions to achieve better fit.

Our chemical network was expanded from the network used by Mullikin et al. (2021). The photodissociation processes for O, O_2, and O_3 were updated to include every possible dissociation pathway, including pathways to ionic products. Ion-neutral reactions involving oxygen were added from Pastina & LaVerne (2001), Anicich (2003), and the NIST Chemistry webbook (NIST 2022). Electron-Ion recombination reactions resulting in suprathermal products ($\mathrm{A}^+ + \mathrm{e}^- \rightarrow \mathrm{A}^*$ and $\mathrm{A}^+ + \mathrm{e}^- \rightarrow \mathrm{B}^* + \mathrm{C}^*$) were added for all of the corresponding P1 processes. Ion-recombination reactions to single and multiple suprathermal products ($\mathrm{A}^+ + \mathrm{B}^- \rightarrow \mathrm{C}^* + \mathrm{D}^*$) were also added into the network. A list of photo processes and reactions included in the network can be found in Appendix A.

3.2 Model

We used the MONACO model developed by Vasyunin et al. (2017) written in Fortran 90. The code was modified to account for irradiation chemical reactions on and in ice using the SH method (Shingledecker & Herbst 2018). This method uses a modified rate equation method for reactions in the grain ice mantle that describes the evolution of the abundance of each species in the network and accounts for electronically excited suprathermal species produced during photoprocessing of ices.

The model treats the ice as being composed of a surface layer defined as the top four monolayers of the ice and the bulk layer. For this project the model was run in a "simulate experiment" mode which limits the physical processes, i.e. cosmic rays, photons from starlight, etc. to those relevant for the system being studied. To model Gerakines et al. (1996), the starting composition of the ice was set to pure O_2 with an ice thickness of 1.0000×10^{-4} cm, a surface area of 1.0000×10^{-20} cm^2, and a volume density of 5.7000×10^{22} cm^{-3} at a temperature of 10.000 K. The ice in our simulation was irradiated by only UV photons at a flux of 1.0000×10^{15} photons/cm^2 s. Additionally, desorption was disabled in the model to mimic the experimental conditions in which the irradiated ice was capped with a layer of noble gas. With these settings we are focusing solely on the bulk reactivity of the ice and are not accounting for surface diffusion or reactivity at the surface-to-gas interface.

3.3 Analysis

The model produces outputs of two different file types. First, .csv files are created for each species, cataloguing fluence in particles/cm^2 and volume density in cm^{-3}. The second output mode is comprised of fixed-width text files referred to as analytics files. These contain a list of every formation and destruction reaction with non-negligible rate for each species in the model. The analytics lists are organized by time-step and repeated for each time step within the modeled parameters. For each

reaction at each time-step the analytics file gives: the total rate of reaction in cm^3/s, the fraction of total production/destruction, the reaction type, and the rate coefficient.

The .csv files were combined so that the data on volume density for each species with respect to fluence was saved in a single pandas dataframe. The analytics files were read into separate pandas dataframes for each species. The time-step, reaction number, and percent contribution to rate of each reaction were recorded and then formatted into a dataframe that contained the fraction of total production or destruction rate for each reaction with respect to the time step using a custom Python script written by the author.

All plots were created using the Matplotlib package in Python.

3.3.1 Agreement with existing experimental data

This model attempts to replicate the results of Gerakines et al. (1996) who performed UV photolysis experiments on samples of pure ices at 10 K. To compare to the results of our model, the experimental data was scaled as in Mullikin et al. (2021). The volume density of O_3 in the bulk as given by our model was scaled along the y-axis as

$$\frac{3 \times n_{O_3}}{n_{O_2,initial}} \times 100\%. \tag{18}$$

where n_A is the volume density of species A. Fluence, displayed along the x-axis, required no scaling. The data from our model was then plotted with respect to fluence on a log-log plot against the results from Mullikin et al. (2021) and the experimental data from Gerakines et al. (1996) as shown in Section 4.1

3.3.2 Ion Abundances

To determine the total ion abundance in the bulk of the ice at each fluence, the volume density of each ionic species was summed and then divided by the initial

volume density of O_2 and multiplied by 100%.

$$\frac{\sum n_{ionic\ species}}{n_{O_2,initial}} \times 100\% \tag{19}$$

This was then plotted with respect to fluence against the abundance of individual ions, scaled similarly, on a log-log plot as shown in Section 4.2.

3.3.3 Reaction Contributions

Because the analytics files give time-steps rather than fluences, the fluence was calculated by multiplying a time-step by the flux of the UV photons, 1.0000×10^{15} photons/cm^2 s. The percent contribution of a reaction to the overall rate is given by

$$\left(\frac{\mathrm{d}X}{\mathrm{d}t} \middle/ \sum^{N} \left| \frac{\mathrm{d}X_n}{\mathrm{d}t} \right| \right) \times 100\%$$

If a reaction contributed less than 5% to the reaction rate at all time steps, it was omitted from the plot. Reactions were categorized into neutral-neutral reactions, ion-neutral reactions, ion recombination reactions, photoprocesses, and quenching reactions, each being plotted with a different line style. This information was plotted with respect to fluence on a linear-log plot for each species.

4 RESULTS

The purpose of this project is to determine if ion-neutral reactivity plays a significant role in the chemical processes in irradiated interstellar ices. First, we ensured that the model output agreed with published experimental results (Section 4.1) and that the ion abundances within the ice were plausible (Section 4.2). We then examined the major formation and destruction pathways as given by the model to determine which types of reactions contribute the most to the rate (Section 4.3). Finally we will show that this approach is scalable to more complex ices (Section 4.4).

4.1 Agreement with existing experimental data

We've added ion-neutral and ion-ion reactions to the model. By comparing experimental data, as described in Shingledecker et al. (2019) and Mullikin et al. (2021), we can gauge if our model is a reasonable hypothesis for which reactions are occurring at what rates, and which types of reactions are most important to the chemistry in irradiated ices. To compare to the experiment we plot the abundance of ozone predicted by our model to the abundance of ozone observed in the irradiation of a film of pure O_2 ice done by Gerakines et al. (1996). Gerakines et al. (1996) performed UV photolysis experiments on pure 10 K samples of nine ices, including pure O_2 ice, and tracked the production of ozone (O_3) which was the solitary observed photolysis product. We compare the results of our model with their observed abundances to gauge the accuracy of our model.

As can be seen from Figure 7, our model, given by the blue curve, has very good agreement on steady-state abundances. From this it can be inferred that our chemical network and associated photo-rates capture the steady state chemistry of the system, after the terminal abundance of ozone has been obtained. Before steady state, the our calculated results differ more from the experimental data. From the standpoint of the chemical network, our reproduction of the steady state, but not the time-varying,

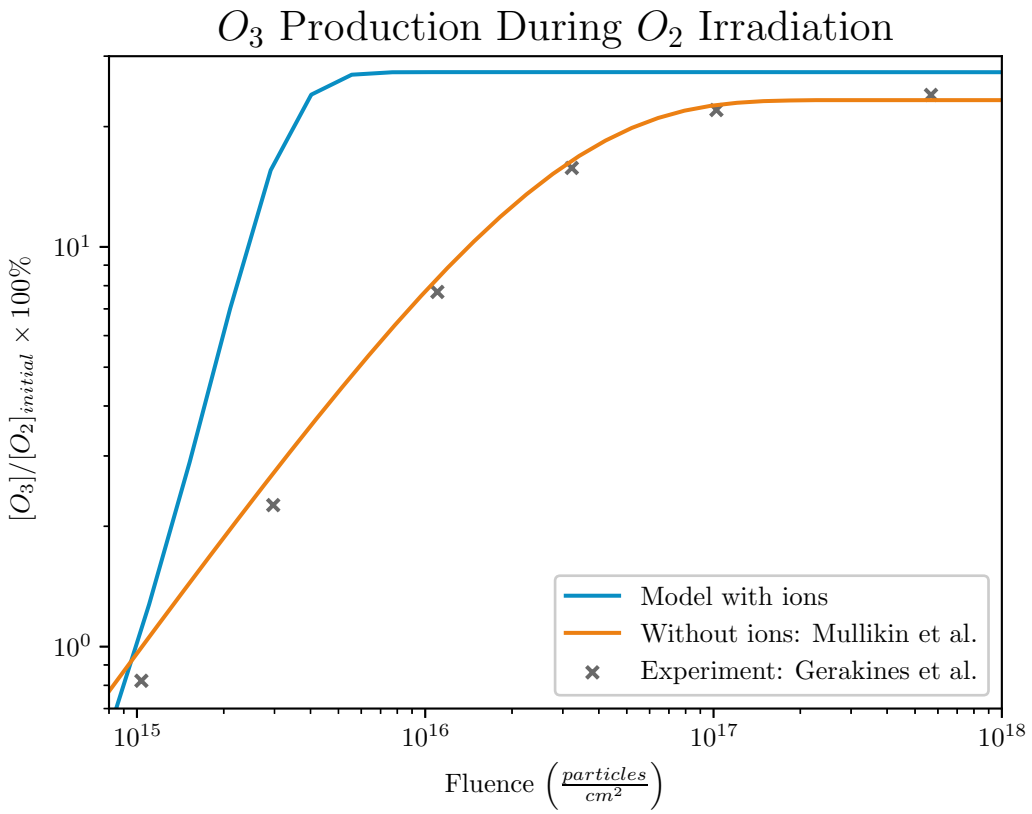

Fig. 7: O_3 Production During O_2 Irradiation Shown is the fit of the model, in blue, against the experimental data (Gerakines et al. 1996) and an earlier version of the model (Mullikin et al. 2021) that did not include ions, in orange. The x-axis is $\log_{10}$ Fluence (flux multiplied by time) and the y-axis is the log of the percentage of the ice composed of ozone (O_3). Note that at steady state the blue line is a good order of magnitude fit but we reach steady state more quickly than the experiment.

abundance of ozone suggests that we have included overall the key reactions and rates for the production of O_3, but that the the values of other processes leading to steady state require further refinement.

In order to obtain this agreement, the rate constants for ion-neutral and ion-ion reactions were of the order $10^{-20}\,\mathrm{cm}^3/\mathrm{s}$, which interestingly is substantially slower than that used for neutral species which is of the order $10^{-8}\,\mathrm{cm}^3/\mathrm{s}$. Though the rate of ion-neutral and ion-ion reactions has been artificially slowed by this method,

overall our photolysis rates are evidently still too fast, as shown by steady state being achieved at smaller fluences in our model than in the experiment.

Good agreement as a function of fluence is determined by the way in which we are reaching steady state, and asks the question, "are we reaching steady state at the same time as the experiment?" Our fit is qualitatively close in that we see the same shape and timing in the formation of ozone, it just reaches steady state more quickly than in the experiment. This indicates that we are missing something in the way we calculate the rate of ion neutral reactions. In the model we treat these reactions as barrierless; if they are not barrierless this could account for the issue. While this is much better than the traditional qualitative agreement that is typically accepted in this field, with fine tuning of the delta values, we expect to obtain exact agreement with the experiment, as seen in Mullikin et al. (2021), where they used an oxygen ice network that did not include ions.

4.2 Ion Abundances

As this is the first model to explicitly look at the ion reactivity in the ice, it is important that we look at the ion abundances in the ice over the course of the runtime. In Figure 8, ion abundances are depicted as a percentage of the ice and we can see that the steady state abundance of the sum total of all the ionic species is approximately 5% if the species in the ice. Unfortunately, to the best of our knowledge, there does not exist experimental data with which to compare these results, however if the ions behave similarly to radicals (Greenberg & Yencha 1973) then a 5% ion abundance seems to be within the realm of physical possibility.

Initially O^+ and O^- are the most abundant ions, but at steady state $O_3{}^-$ is the most abundant ion. This is likely because the primary formation pathway of $O_3{}^-$ is the ion-neutral reaction $\mathbf{O_2 + O^- \rightarrow O_3{}^-}$ (See Section 4.3.3.3), while O^- is initially formed through the photodissociation of the plentiful O_2 (see Section 4.3.3.1).

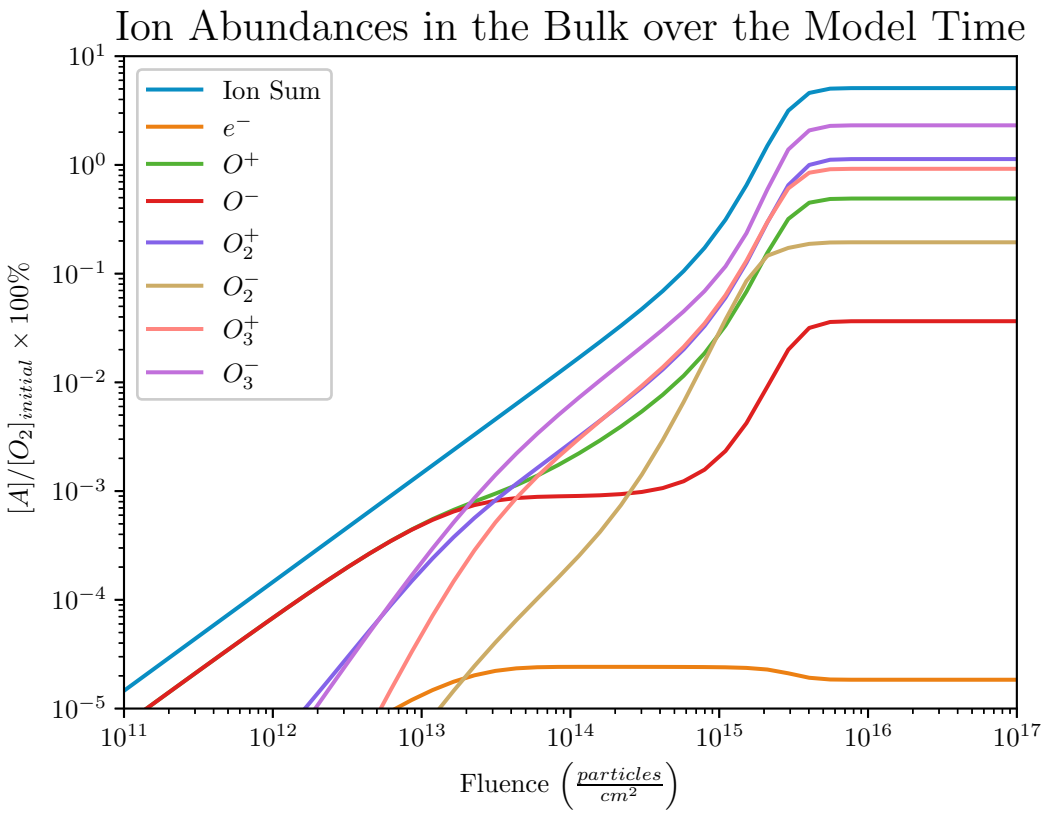

Fig. 8: Ion abundance The log of the fractional ion abundance with respect to $\log_{10}$ fluence. At steady state the ionic species make up approximately 5% of the ice. Initially O^+ and O^- are the most abundant ions, but at steady state $O_3{}^-$ is the most abundant ion.

It may be possible to look at sputtered ions to determine which ions are present in the ice, however this would not tell their relative abundances in the ice or to each other. Sputtering is a potentially important mechanism for gas-grain interface dynamics, but an investigation of sputtering falls beyond the scope of the current work. We hope this motivates people to further examine this and try to better constrain the ion fraction within the ice as a function of irradiation time.

4.3 Reaction Contributions

Because the model demonstrates good fit with the experimental data while estimating ion abundances within expectations, the reactions predicted by the model

likely carry significant implications for astrochemical analysis. In Figures 7 and 8 the percent abundance of each species is plotted against fluence. In this section we will be looking at what reactions contribute to that abundance for each species.

Figure 9 shows the contribution of each reaction to the rate of formation of each species in the network as a function of fluence. Only reactions that account for more than 5% of the rate at any point are included. The y-axis is described as

$$\left(\frac{\mathrm{d}X}{\mathrm{d}t} \Bigg/ \sum^{N} \left| \frac{\mathrm{d}X_{\mathrm{n}}}{\mathrm{d}t} \right| \right) \times 100\% \tag{20}$$

where $\frac{\mathrm{d}X}{\mathrm{d}t}$ is the rate of the reaction plotted, and the x-axis is fluence. Early fluences describe the time period in which the ice is primarily O_2 and there aren't enough other things to affect the rate. Middle fluences describe the time period in which other species have formed in high enough concentrations to begin to affect the rates. Late fluences describe the system in steady-state. The type of reaction is depicted by linestyle as described in Table 1.

Linestyle	Reaction Type
———	neutral-neutral
- - - - -	ion-neutral
-·-·-·	ion recombination
·····	photoprocesses
-···-··	quenching

Table 1: Linestyle Legend In Figure 9 a solid line indicates a neutral-neutral reaction, a dashed line indicates an ion-neutral reaction, a dash-dotted line indicates an ion-ion reaction, a dotted line indicates a photo process and a dash-dot-dot-dotted line indicates a quenching process.

4.3.1 Neutrals

4.3.1.1 Formation of O

The contributions of each reaction to the rate of formation of O is shown in Figure 9a. At early fluences the rate of formation of O is governed by the photodissociation via photoexcitation reaction $O_2 \rightsquigarrow 2O$. As more species form in the ice, the ion-neutral reactions, $O^+ + O_2 \rightarrow {O_2}^+ + O$ and ${O_2}^+ + O_2 \rightarrow {O_3}^+ + O$, become the

(a) Formation of O

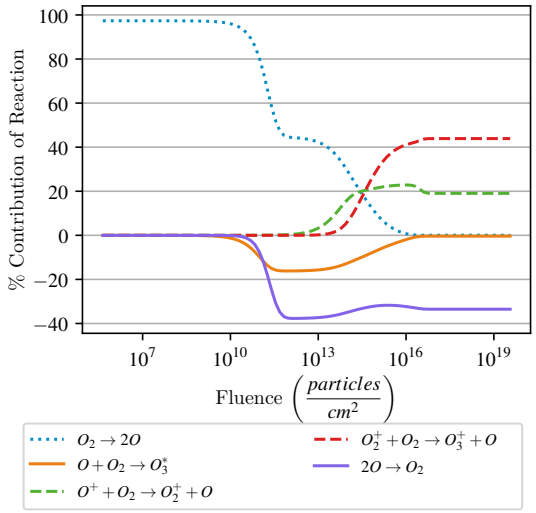

(b) Formation of O_2

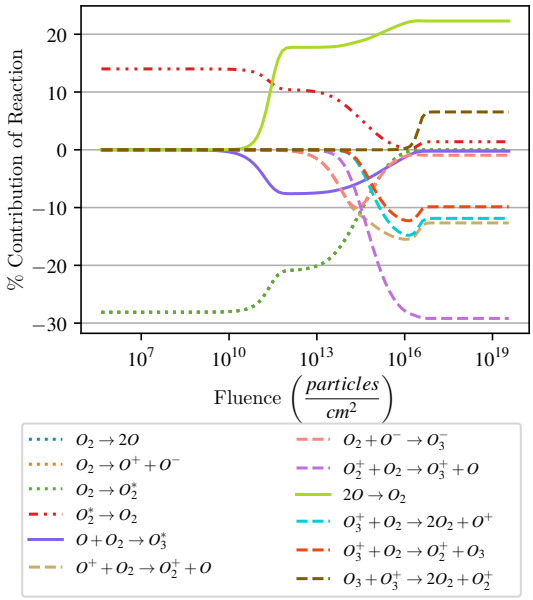

(c) Formation of O_3

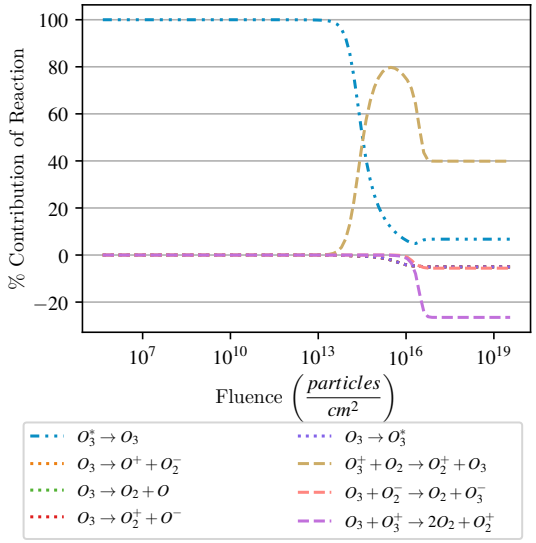

(d) Formation of O^+

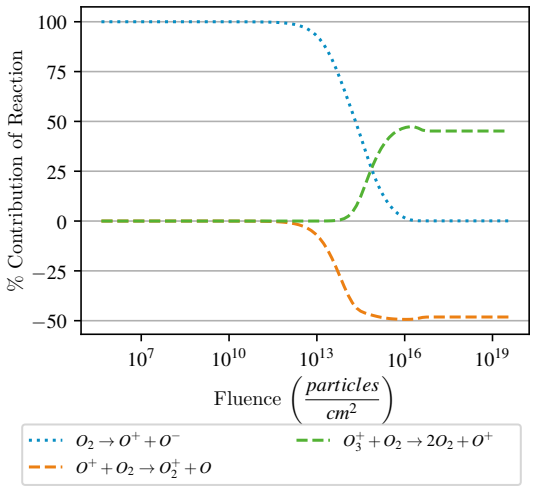

Fig. 9: Reaction Contributions to Rate of Formation of Network Species The contribution of each reaction to the rate of formation of each species in the network as a function of fluence. Full size figures are located in Appendix B

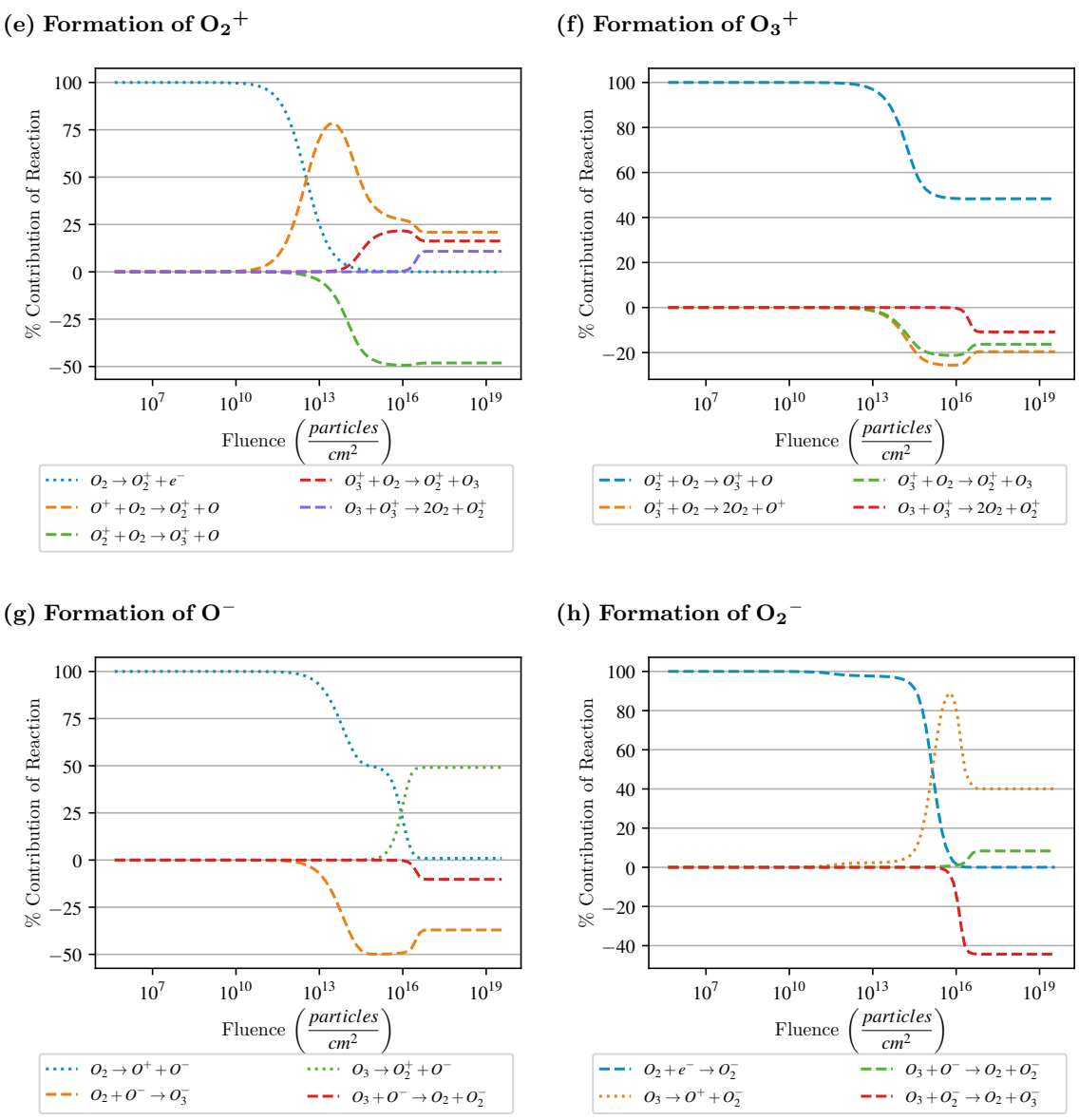

Fig. 9: Reaction Contributions to Rate of Formation of Network Species cont.

major formation pathways. The destruction pathways of O during the middle fluences are governed by the neutral-neutral reactions $O + O_2 \rightarrow O_3^*$ and $2O \rightarrow O_2$ and the rate contribution of former goes to zero at late fluences.

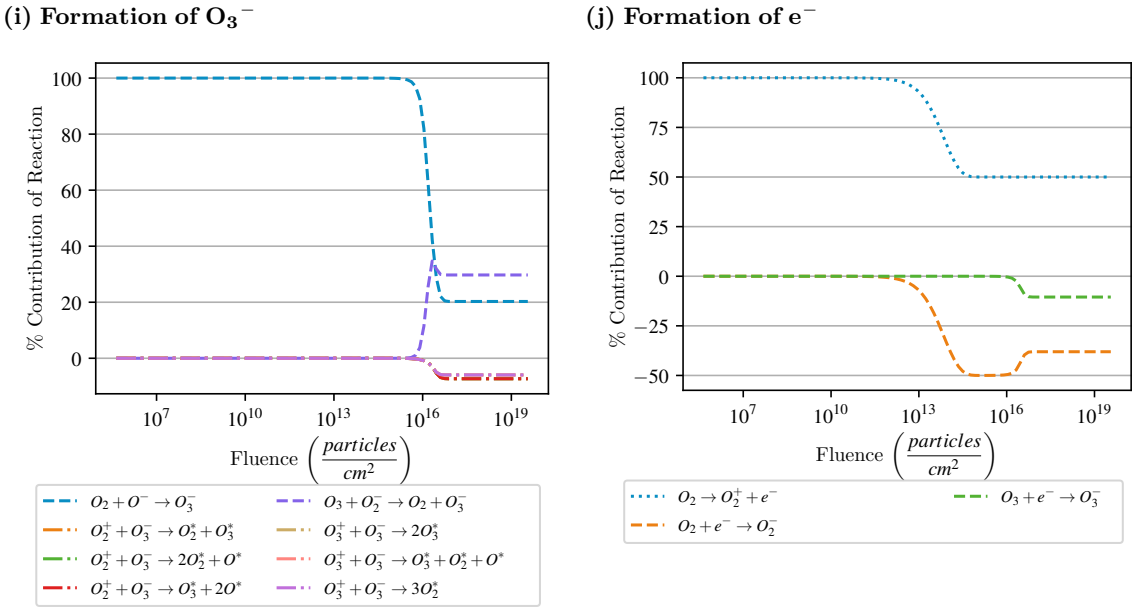

Fig. 9: Reaction Contributions to Rate of Formation of Network Species cont.

4.3.1.2 Formation of O_2

The contributions of each reaction to the rate of formation of O_2 is shown in Figure 9b. At the start of our simulations, the ice is composed of entirely O_2 ice. At early fluences the three primary destruction pathways are the photoexcitation and photoionization processes, $O_2 \rightsquigarrow 2O$, $O_2 \rightsquigarrow O^+ + O^-$, and $O_2 \rightsquigarrow O_2^*$. The primary formation pathway at early fluences is the quenching reaction, $O_2^* \rightarrow O_2$. As the cations form in the ice, ion-neutral reactions become the major destruction pathways so that at late fluences the major destruction pathways are $O_2^+ + O_2 \rightarrow O_3^+ + O$, $O^+ + O_2 \rightarrow O_2^+ + O$, $O_3^+ + O_2 \rightarrow 2O_2 + O^+$ and $O_3^+ + O_2 \rightarrow O_2^+ + O_3$. At late fluences the primary formation pathway is the neutral-neutral reaction, $2O \rightarrow O_2$, with the ion-neural reaction, $O_3^+ + O_3 \rightarrow 2O_2 + O_2^+$, contributing non-negligibly to the formation of O_2.

4.3.1.3 Formation of O_3

The contributions of each reaction to the rate of formation of O_3 is shown in Figure 9c. At early fluences the rate of formation of ozone is governed by the quenching reaction, $O_3{}^* \rightarrow O_3$, where $O_3{}^*$ forms mainly via $O + O_2 \rightarrow O_3{}^*$. However, at middle fluences the ion-neutral reaction, $O_3{}^+ + O_2 \rightarrow O_2{}^+ + O_3$ becomes the major formation pathway. At late fluences, the destruction of ozone is primarily through an ion-neutral pathway, $O_3{}^+ + O_3 \rightarrow 2O_2 + O_2{}^+$, or one of four photoprocesses, $O_3 \rightsquigarrow O^+ + O_2{}^-$, $O_3 \rightsquigarrow O_2 + O$, $O_3 \rightsquigarrow O_2{}^+ + O^-$, or $O_3 \rightsquigarrow O_3{}^*$.

4.3.2 Cations

4.3.2.1 Formation of O^+

The contributions of each reaction to the rate of formation of O^+ is shown in Figure 9d. At early fluences the formation of O^+ is governed by the photoexcitation reaction, $O_2 \rightsquigarrow O^+ + O^-$. At steady state both major formation and destruction pathways are ion-neutral reactions, $O_3{}^+ + O_2 \rightarrow 2O_2 + O^+$ and $O^+ + O_2 \rightarrow O_2{}^+ + O$. Recombination reactions each contribute a negligible ($< 1\%$) amount to the rate.

4.3.2.2 Formation of $O_2{}^+$

The contributions of each reaction to the rate of formation of $O_2{}^+$ is shown in Figure 9e. At early fluences the formation of $O_2{}^+$ is governed by the photoionization reaction, $O_2 \rightsquigarrow O_2{}^+ + e^-$. At middle and late fluences, all major formation and destruction pathways are ion-neutral reactions, $O^+ + O_2 \rightarrow O_2{}^+ + O$, $O_3{}^+ + O_2 \rightarrow O_2{}^+ + O_3$, $O_3{}^+ + O_3 \rightarrow 2O_2 + O_2{}^+$, and $O_2{}^+ + O_2 \rightarrow O_3{}^+ + O$. Recombination reactions each contribute a negligible ($< 0.5\%$) amount to the rate.

4.3.2.3 Formation of $O_3{}^+$

The contributions of each reaction to the rate of formation of $O_3{}^+$ is shown in Figure 9f. At all fluences, ion-neutral reactions are the major formation

($O_2^+ + O_2 \rightarrow O_3^+ + O$) and destruction ($O_3^+ + O_2 \rightarrow 2O_2 + O^+$, $O_3^+ + O_2 \rightarrow O_2^+ + O_3$, and $O_3^+ + O_3 \rightarrow 2O_2 + O_2^+$) pathways of O_3^+. Recombination reactions each contribute a negligible ($< 0.5\%$) amount to the rate.

4.3.3 Anions

4.3.3.1 Formation of O^-

The contributions of each reaction to the rate of formation of O^- is shown in Figure 9g. The formation of O^- is governed by photoexcitation reactions. At early fluences it is the photodissociation of O_2, $O_2 \rightsquigarrow O^+ + O^-$, but at steady state it is the photodissociation of O_3, $O_3 \rightsquigarrow O_2^+ + O^-$. Both major destruction pathways are ion-neutral reactions, $O_2 + O^- \rightarrow O_3^-$ and $O_3 + O^- \rightarrow O_2 + O_2^-$. Recombination reactions each contribute a negligible ($< 1.3\%$) amount to the rate.

4.3.3.2 Formation of O_2^-

The contributions of each reaction to the rate of formation of O_2^- is shown in Figure 9h. At early fluences O_2^- is formed via the ion-neutral reaction, $O_2 + e^- \rightarrow O_2^-$, but as more species are formed the photodissociation of O_3, $O_3 \rightsquigarrow O^+ + O_2^-$, becomes the major formation pathway. Recombination reactions each contribute a negligible ($< 1.5\%$) amount to the rate.

4.3.3.3 Formation of O_3^-

The contributions of each reaction to the rate of formation of O_3^- is shown in Figure 9i. At early fluences O_3^- is formed via the ion-neutral reaction $O_2 + O^- \rightarrow O_3^-$. At late fluences, this reaction accounts for slightly less of the formation than another ion-neutral reaction, $O_3 + O_2^- \rightarrow O_3 + O_3^-$. The destruction of O_3^- occurs entirely through recombination reactions. Please note that in the figure the six recombination reactions are plotted on top of each other in the pink and red dash-dotted lines.

4.3.4 Electrons

The contributions of each reaction to the rate of formation of the electrons is shown in Figure 9j. Electrons are entirely produced in the photoionization of O_2, $O_2 \rightsquigarrow {O_2}^+ + e^-$. They are consumed in ion-neutral reactions with O_2 and O_3. Recombination reactions each contribute a negligible ($< 0.5\%$) amount to the rate.

4.3.5 In Summary

For all species the rate contributions at early fluences are dominated by photoprocesses and quenching reactions with the exception of ${O_3}^+$, ${O_2}^-$, and ${O_3}^-$ whose rates are each dominated by an ion-neutral reaction involving O_2. This makes sense because at early fluences O_2 is very abundant. At late fluences an ion-neutral reaction is the largest contributor to the rate of the neutral species (for O_2 its a destruction reaction).

It is worth noting that in the model that includes only neutral species, seen in Mullikin et al. (2021), this shift of which reactions are important does not occur and the reactions that were the major formation/destruction pathways at early fluences remains the major pathways at steady state.

4.4 Scalability

Runtime information for the model with and without including ions is shown in Table 2. As you can see, the runtime did not increase with the addition of ions and the maximum amount of memory used at any time by any process in that job (MaxRRS) had only a negligible increase. This means that our approach is scalable to even more complex reaction networks.

	Without Ions		With Ions	
Bulk Species	3		10	
Bulk Photoprocesses	8		13	
Bulk Two-body Reactions	2		43	
JobName	batch	extern	batch	extern
MaxRRS	1472K	1324K	1608K	1320K
Time Elapsed	00:00:02	00:00:02	00:00:02	00:00:02

Table 2: Runtime Comparison Table containing the runtime information for two runs of the model. The first used the original neutral-only network, the second used my expanded network that includes ions. The runtime did not increase and use of memory had only a negligible increase.

5 DISCUSSION

An irradiated pure O_2 ice represents arguably the simplest possible system with which to test our new approach, since oxygen does not polymerize into arbitrarily large molecules, unlike, e.g. carbon. Nevertheless, our preliminary results described here, we hope, provide compelling evidence for the importance of solid-phase ion-ice interactions. Moreover, our approach is in principle easily extended to more complex systems, which will be a major avenue of future work with this model. Finally, it is our hope that these results will facilitate future research on molecular behavior in irradiated ices.

As shown in Figure 7, simulations using the input parameters given in Appendix A yield calculated abundances in good agreement with experimental data. Moreover, while no experimental data on ion abundances within irradiated ices are available in the literature to the best of our knowledge, the total solid phase ion abundance of 5% predicted by our models seems reasonable. The combination of this fit and abundance allowed the reaction contributions determined by our model to serve as an initial estimate of reactivity within the bulk of interstellar ices in cold dense cores.

As seen in Figure 9, ion-neutral reactions contribute significantly to both the formation and destruction pathways of molecular species within the bulk of irradiated O_2 ice. These results provide compelling evidence that ice models must account for ion-neutral reactivity in their chemical networks if they are to accurately mimic the processes occurring within cosmic ice.

Of course, there remain several significant challenges to modeling ionic behavior. Primary among these challenges is the lack of experimental data on ion-neutral reactivity in irradiated ices and the lack of data on the activation energies of such ion-neutral reactions. Therefore, in this model we had to treat ionic species as a

hybrid between ground state species (with normal activation energy barriers) and suprathermal species (with no activation energy barriers).

As is typically the case with gas-phase reactions in astrochemical models (Herbst & Klemperer 1973), this model considers a reaction involving an ion to occur barrierlessly. In our code, this behaviour is implemented by treating solid-phase ions as analogous to solid-phase suprathermal species. However, this treatment meant that the model reached steady state much more rapidly than the experiment. To account for this our code sets the ions' vibrational frequencies to $700\,\mathrm{s}^{-1}$, thus artificially slowing the reactions. The slower vibrational frequency attempts to remove the assumption that a reaction involving an ion occurs barrierlessly, and account for the unknown activation energies of the ionic species.

This results in a rate constant of the order $10^{-8}\,\mathrm{cm}^3/\mathrm{s}$ for neutral reactions and a rate constant of the order $10^{-20}\,\mathrm{cm}^3/\mathrm{s}$ for ion-neutral and ion-ion reactions. It is interesting to note that even though they have the same rate constant as the ion-neutral reactions, which are quite often primary formation/destruction pathways, the rates of the ion-ion recombination reactions are much lower. The reason become apparent when we recall that for the reaction

$$A + B \xrightarrow{k} \text{products}, \tag{21}$$

the rate is given by

$$\text{Rate} = k[A][B]. \tag{22}$$

The greater abundance of neutral reactants causes the rate of ion-neutral reactions to be greater than the rate of ion-ion recombination reactions.

If we were to follow Eq. 17, the ion-neutral rate constant would be expected to fall within the same order of magnitude as the neutral-neutral rate constant. Within the

current model however, we instead used an adjustable parameter within the rate constants of reactions involving an ion in order to artificially slow them to better match the experimental data currently available. As additional experimental data is gathered on the reaction barriers for ionic species, we would like to revise the model to account for these factors directly.

We find that ion-neutral chemistry provides important barrierless pathways for non-diffusive bulk-phase reactivity, similarly to what occurs when ions are found in the gas phase (Herbst & Klemperer 1973). Consequently, ion-neutral reactions represent an astrophysically important mechanism for driving chemical change in cosmic ices even at the low temperatures characteristic of dense molecular clouds ($\sim$10 K).

The behavior of ion-neutral reactions in the solid phase of cosmic ices has long-awaited exploration due to the complexity of the underlying chemistry. Nevertheless, as we have shown, data for ionic behavior can reasonably be coded into astrochemical models without becoming excessively computationally demanding. The importance of ion-neutral pathways to both the formation and destruction pathways of the neutral species in our chemical network found by our model indicates that it is indeed erroneous to assume that solid-phase ions contribute only negligibly to bulk chemistry. It is clear that the addition of ionic behavior to the network provides a more complex, and likely more accurate, depiction of the chemistry occurring within irradiated ices.

6 CONCLUSIONS

In this project, we have for the first time added ion-neutral chemistry to an irradiated ice chemistry model, thus finding that ion-neutral chemistry contributes significantly more to solid phase reactivity than previously assumed. From this we conclude that ionic chemistry should no longer be neglected in solid-phase ice models, despite the challenges of complexity that have hindered the inclusion of ions thus far. As our network examines more complicated ices and more experimental data is incorporated into the model, the delta values will undoubtedly change. By incorporating better parameters into the model and and more experimental data, we hope to find a set of consistent delta values that will allow this astrochemical model to become predictive rather than descriptive. Adjusting the starting conditions of such a model— temperature, flux, density, etc.—will allow us to predict rather than explain the reactivity found in the regions of space examined by new telescopes such as the JWST.

While at an early stage of development, we believe that the fit of the current model is sufficiently close to the experimental findings to give a general idea of what ionic chemistry occurs in irradiated ices. This project is therefore a confident first step towards determining which types of reactions should be included within a predictive model—a step which we aim to improve upon through additional experimentation.

7 FUTURE WORK

With the recent launch of the JWST, many previously hidden areas of the universe are now available to be mapped and explored. It is therefore more important than ever to have models that can accurately describe the chemistry of the particles found in these new regions. While current models have neglected how ionic behavior informs solid-phase chemistry in the bulk of cosmic ices, the model we have developed demonstrates a method toward integrating more complex molecular data into chemical networks.

In this work we have focused on the simplest possible system, the bulk of irradiated O_2 ice. However, the novel approach to including ions described in this work, coupled with an automated program for determining delta values currently in development, will allow us to extend these results to more complex systems such as H_2O, CO, and CH_3OH, the dominant constituent of interstellar dust-grain ice mantles.

Future work in this area will need to examine the barriers to ion-neutral reactions. The assumption that ion-neutral reactions proceed barrierlessly remains a continuing source of uncertainty, because our results clearly indicate that while ion-neutral reactions do occur faster than neutral-neutral reactions, they do not occur with the same speed expected from barrierless suprathermal reactions. It would also be helpful to know about the ion abundances in irradiated ices in order to better constrain the model. Experimental research can help to answer questions about time-dependent ion fractions within ice.

While the current project has focused on modeling non-diffusive bulk chemistry, our work also has implications for another major process relevant to cosmic ices: namely, the interface dynamics between the ice surface and the surrounding gas. We would like to study the interface dynamics, specifically desorption (See Figure 5),

because it could help us to better understand how species we have observed in the gas of molecular clouds, but which likely formed on dust-grains, could have desorbed at the low temperatures of cold dense cores.

Literature Cited

Abplanalp, M. J., Frigge, R., & Kaiser, R. I. 2019, Science Advances, 5, eaaw5841, doi: 10.1126/sciadv.aaw5841

Acharyya, K., Schulte, S. W., & Herbst, E. 2020, The Astrophysical Journal Supplement Series, 247, 4, doi: 10.3847/1538-4365/ab6599

Allen, M., & Robinson, G. W. 1977, The Astrophysical Journal, 212, 396, doi: 10.1086/155059

Anicich, V. G. 2003, An index of the literature for bimolecular gas phase cation-molecule reaction kinetics, Tech. rep., NASA. https://trs.jpl.nasa.gov/handle/2014/7981

Arumainayagam, C. R., Garrod, R. T., Boyer, M. C., et al. 2019, Chemical Society Reviews, 48, 2293, doi: 10.1039/C7CS00443E

Baragiola, R. A., Atteberry, C. L., Bahr, D. A., & Jakas, M. M. 1999, Nuclear Instruments and Methods in Physics Research Section B: Beam Interactions with Materials and Atoms, 157, 233. http://www.sciencedirect.com/science/article/pii/S0168583X99004310

Boogert, A. A., Gerakines, P. A., & Whittet, D. C. 2015, Annual Review of Astronomy & Astrophysics, 53, 541, doi: 10.1146/annurev-astro-082214-122348

Butterfield, N., Battersby, C., Ginsburg, A., Mills, E., & Dunnagan, R. 2021, in American Astronomical Society Meeting Abstracts, Vol. 53, American Astronomical Society Meeting Abstracts, 131.06

CDMS. 2019, Cologne Database for Molecular Spectroscopy, https://cdms.astro.uni-koeln.de/

Collings, M. P., Anderson, M. A., Chen, R., et al. 2004, Monthly Notices of the Royal Astronomical Society, 354, 1133, doi: 10.1111/j.1365-2966.2004.08272.x

Cuppen, H. M., Fredon, A., Lamberts, T., et al. 2018, IAU Symposium, 332, 293, doi: 10.1017/S1743921317009929

Dalgarno, A. 2008, Annual Review of Astronomy & Astrophysics, 46, 1, doi: 10.1146/annurev.astro.46.060407.145216

Draine, B. 2010, Physics of the Interstellar and Intergalactic Medium, Princeton Series in Astrophysics (Princeton University Press). https://books.google.com/books?id=FycJvKHyiwsC

Erickson, E. F. 1992, Space Science Review, 61, 61, doi: 10.1007/BF00212475

Evans, Neal J., I., Rawlings, J. M. C., Shirley, Y. L., & Mundy, L. G. 2001, The Astrophysical Journal, 557, 193, doi: 10.1086/321639

Fraser, H. J., McCoustra, M. R. S., & Williams, D. A. 2002, Astronomy and Geophysics, 43, 2.10, doi: 10.1046/j.1468-4004.2002.43210.x

Gardner, J. P., Mather, J. C., Clampin, M., et al. 2006, Space Science Review, 123, 485, doi: 10.1007/s11214-006-8315-7

Garrod, R. T., & Herbst, E. 2006, Astronomy & Astrophysics, 457, 927, doi: 10.1051/0004-6361:20065560

Garrod, R. T., Weaver, S. L. W., & Herbst, E. 2008, The Astrophysical Journal, 682, 283, doi: 10.1086/588035

Gerakines, P. A., Schutte, W. A., & Ehrenfreund, P. 1996, Astronomy & Astrophysics, 312, 289

Gibb, E. L., Whittet, D. C. B., Boogert, A. C. A., & Tielens, A. G. G. M. 2004, The Astrophysical Journal Supplement Series, 151, 35, doi: 10.1086/381182

Gomis, O., Leto, G., & Strazzulla, G. 2004, Astronomy & Astrophysics, 420, 405, doi: 10.1051/0004-6361:20041091

Greenberg, J. M., & Yencha, A. J. 1973, in Interstellar Dust and Related Topics, ed. J. M. Greenberg & H. C. van de Hulst, 52, 369

Guevara, C., Stutzki, J., Ossenkopf-Okada, V., et al. 2020, Astronomy & Astrophysics, 636, A16, doi: 10.1051/0004-6361/201834380

Hasegawa, T. I., & Herbst, E. 1993, Monthly Notices of the Royal Astronomical Society, 261, 83

Hasegawa, T. I., Herbst, E., & Leung, C. M. 1992, The Astrophysical Journal Supplement Series, 82, 167, doi: 10.1086/191713

Heays, A. N., Bosman, A. D., & Dishoeck, E. F. v. 2017, Astronomy & Astrophysics, 602, A105, doi: 10.1051/0004-6361/201628742

Herbst, E., & Klemperer, W. 1973, The Astrophysical Journal, 185, 505, doi: 10.1086/152436

Herbst, E., & Millar, T. J. 2008, in Low Temperatures and Cold Molecules, ed. I. W. M. Smith (London: Imperial College Press)

Herbst, E., & van Dishoeck, E. F. 2009, Annual Review of Astronomy & Astrophysics, 47, 427, doi: 10.1146/annurev-astro-082708-101654

Herzberg, G. 1950, Molecular Spectra and Molecular Structure I. Spectra of Diatomic Molecules (Princeton, New Jersey: D.Van Nostrand Company Inc.). https://archive.org/details/molecularspectra032774mbp/mode/2up

Ho, P. T. P., & Townes, C. H. 1983, Annual Review of Astronomy & Astrophysics, 21, 239, doi: 10.1146/annurev.aa.21.090183.001323

Hogerheijde, M. R. 2005, Chemical Evolution of Protostars, ed. W. A. Baan, Y. Hagiwara, & H. J. van Langevelde, 179, doi: 10.1007/1-4020-3831-3_21

Ishiguro, M. 2001, Astronomical Herald, 94, 567

Jakobsen, R., & Laurance, R. J. 1989, ESA Bulletin, 58, 91

Kessler, M. F., Steinz, J. A., Anderegg, M. E., et al. 1996, Astronomy & Astrophysics, 500, 493

Kleimeier, N. F., Abplanalp, M. J., Johnson, R. N., et al. 2021, The Astrophysical Journal, 911, 24, doi: 10.3847/1538-4357/abdec3

Lemonick, S. 2021, Chemical & Engineering News. https://cen.acs.org/physical-chemistry/astrochemistry/James-Webb-Space-Telescope-astrochemistsnewest/99/i41

Lewis, J. S. 1974, Science, 186, 440, doi: 10.1126/science.186.4162.440

McCray, R., & Dalgarno, A. 1972, in Bulletin of the American Astronomical Society, 4, 225

McGuire, B. A. 2022, The Astrophysical Journal Supplement Series, 259, 30, doi: 10.3847/1538-4365/ac2a48

Mullikin, E., Anderson, H., O'Hern, N., et al. 2021, The Astrophysical Journal, 910, 72, doi: 10.3847/1538-4357/abd778

NIST. 2022, National Institute of Standards and Technology (NIST) Chemistry WebBook, https://webbook.nist.gov/

Öberg, K. I., Fayolle, E. C., Cuppen, H. M., van Dishoeck, E. F., & Linnartz, H. 2009, Astronomy & Astrophysics, 505, 183, doi: 10.1051/0004-6361/200912464

Pastina, B., & LaVerne, J. A. 2001, The Journal of Physical Chemistry A, 105, 9316, doi: 10.1021/jp012245j

Penteado, E. M., Walsh, C., & Cuppen, H. M. 2017, The Astrophysical Journal, 844, 71, doi: 10.3847/1538-4357/aa78f9

Pickles, J. B., & Williams, D. A. 1977, , 52, 443, doi: 10.1007/BF01093879

Prasad, S. S., & Tarafdar, S. P. 1983, Astrophysical Journal, 267, 603, doi: 10.1086/160896

Raut, U., Loeffler, M. J., Famá, M., & Baragiola, R. A. 2011, The Journal of Chemical Physics, 134, 194501, doi: 10.1063/1.3589201

Rybicki, G., & Lightman, A. 2008, Radiative Processes in Astrophysics, Physics textbook (Wiley). https://books.google.com/books?id=eswe2StAspsC

Saunders, J. B., & Bruening, R. J. 1968, Astronomical Journal, 73, 415, doi: 10.1086/110645

Shingledecker, C. N., & Herbst, E. 2018, Physical Chemistry Chemical Physics (Incorporating Faraday Transactions), 20, 5359, doi: 10.1039/C7CP05901A

Shingledecker, C. N., Vasyunin, A., Herbst, E., & Caselli, P. 2019, The Astrophysical Journal, 876, 140, doi: 10.3847/1538-4357/ab16d5

Splatalogue. 2012, Spatalogue database for astronomical spectroscopy, https://splatalogue.online/

Theulé, P., Duvernay, F., Danger, G., et al. 2013, Advances in Space Research, 52, 1567, doi: 10.1016/j.asr.2013.06.034

Tielens, A. G. G. M., & Hagen, W. 1982, Astronomy & Astrophysics, 114, 245

Tofani, G., & Natale, V. 2003, Memorie della Società Astronomica Italiana, 74, 219

van Dishoeck, E. F. 2018, IAU Symposium, 332, 3, doi: 10.1017/S1743921317011528

Vasyunin, A. I., Caselli, P., Dulieu, F., & Jiménez-Serra, I. 2017, The Astrophysical Journal, 842, 33, doi: 10.3847/1538-4357/aa72ec

Wakelam, V., Smith, I. W. M., Herbst, E., et al. 2010, Space Science Review, 156, 13, doi: 10.1007/s11214-010-9712-5

Werner, M. W., Roellig, T. L., Low, F. J., et al. 2004, The Astrophysical Journal Supplement Series, 154, 1, doi: 10.1086/422992

Appendix A

NETWORK

In Table A.1 we show the input parameters for photoprocesses occurring in the network. The branching fraction is the probability that the reaction will proceed in preference to the competing reactions, the cross section is a measure of the probability that the species will absorb a photon with the energy needed for the excitation or ionization process will occur, and the delta value compensates for unknown influences on the rate and is adjusted so that the model agrees with the experimental comparison. The rates of these processes are given by by equations 13-16, repeated here.

$$k_{P1} = P_e \bar{\sigma}_{ion} \Phi \delta, \tag{A.1}$$

$$k_{P2} = (1 - P_e) \bar{\sigma}_{ion} \Phi \delta, \tag{A.2}$$

$$k_{P3} = P_{dis} \bar{\sigma}_{exc} \Phi \delta, \tag{A.3}$$

$$k_{P4} = (1 - P_{dis}) \bar{\sigma}_{exc} \Phi \delta. \tag{A.4}$$

In Table A.2 we show the input parameters for the reactions included in the network. Again the branching fraction is the probability that the reaction will proceed in preference to the competing reactions and E_a is the activation energy required for the reaction. The rates of these reactions are given by equation 17, repeated here.

$$k_{fast} = f_{br} \left[\frac{\nu_0^A + \nu_0^B}{n_{bulk}} \right] \exp\left(-\frac{E_{act}^{AB}}{T_{ice}} \right) \tag{A.5}$$

Only the reactions involved in bulk reactivity are shown.

Table A.1: Photoprocesses

Reaction			Branching Fraction	Cross Section	Delta Value
O	$\overset{PHOEXC}{\rightsquigarrow}$	O*	1.00E+00	0.00E+00	1.00E+00
O	$\overset{PHOION}{\rightsquigarrow}$	$O^+ + e^-$	1.00E+00	0.00E+00	1.00E+00
O_2	$\overset{PHOEXC}{\rightsquigarrow}$	O + O	3.33E-01	2.13E-18	1.00E+01
O_2	$\overset{PHOEXC}{\rightsquigarrow}$	$O^+ + O^-$	3.33E-01	2.13E-18	1.00E+01
O_2	$\overset{PHOEXC}{\rightsquigarrow}$	O_2*	3.33E-01	2.13E-18	1.00E+01
O_2	$\overset{PHOION}{\rightsquigarrow}$	O* + O*	5.00E-01	3.86E-20	1.00E+01
O_2	$\overset{PHOION}{\rightsquigarrow}$	$O_2{}^+ + e^-$	5.00E-01	3.86E-20	1.00E+01
O_3	$\overset{PHOEXC}{\rightsquigarrow}$	$O^+ + O_2{}^-$	2.50E-01	5.60E-18	1.00E+03
O_3	$\overset{PHOEXC}{\rightsquigarrow}$	O_2 + O	2.50E-01	5.60E-18	1.00E+03
O_3	$\overset{PHOEXC}{\rightsquigarrow}$	$O_2{}^+ + O^-$	2.50E-01	5.60E-18	1.00E+03
O_3	$\overset{PHOEXC}{\rightsquigarrow}$	O_3*	2.50E-01	5.60E-18	1.00E+03
O_3	$\overset{PHOION}{\rightsquigarrow}$	O_2* + O*	5.00E-01	0.00E+00	1.00E+00
O_3	$\overset{PHOION}{\rightsquigarrow}$	$O_3{}^+ + e^-$	5.00E-01	0.00E+00	1.00E+00

Table A.2: Reaction Network

Reaction			Branching Fraction	E_a
$O + O$	$\rightarrow$	O_2	5.00E-01	0.0
$O_3 + O_3$	$\rightarrow$	$O_2 + O_2 + O_2$	1.00E+00	9999.0
$O + e^-$	$\rightarrow$	O^-	1.00E+00	0.0
$O + O^-$	$\rightarrow$	${O_2}^-$	1.00E+00	0.0
$O + {O_2}^-$	$\rightarrow$	${O_3}^-$	1.00E+00	0.0
$O^+ + e^-$	$\rightarrow$	O^*	1.00E+00	0.0
$O^+ + O^-$	$\rightarrow$	${O_2}^*$	5.00E-01	0.0
$O^+ + O^-$	$\rightarrow$	$O^* + O^*$	5.00E-01	0.0
$O^+ + O_2$	$\rightarrow$	${O_2}^+ + O$	1.00E+00	0.0
$O^+ + {O_2}^-$	$\rightarrow$	${O_3}^*$	5.00E-01	0.0
$O^+ + {O_2}^-$	$\rightarrow$	$O^* + {O_2}^*$	5.00E-01	0.0
$O^+ + {O_3}^-$	$\rightarrow$	$O^* + {O_3}^*$	5.00E-01	0.0
$O^+ + {O_3}^-$	$\rightarrow$	${O_2}^* + {O_2}^*$	5.00E-01	0.0
$O_2 + e^-$	$\rightarrow$	${O_2}^-$	1.00E+00	0.0
$O_2 + O^-$	$\rightarrow$	${O_3}^-$	1.00E+00	0.0
${O_2}^+ + e^-$	$\rightarrow$	${O_2}^*$	5.00E-01	0.0
${O_2}^+ + e^-$	$\rightarrow$	$O^* + O^*$	5.00E-01	0.0
${O_2}^+ + O^-$	$\rightarrow$	${O_3}^*$	5.00E-01	0.0
${O_2}^+ + O^-$	$\rightarrow$	$O^* + {O_2}^*$	5.00E-01	0.0
${O_2}^+ + O_2$	$\rightarrow$	${O_3}^+ + O$	1.00E+00	0.0
${O_2}^+ + {O_2}^-$	$\rightarrow$	$O^* + {O_3}^*$	5.00E-01	0.0
${O_2}^+ + {O_2}^-$	$\rightarrow$	${O_2}^* + {O_2}^*$	5.00E-01	0.0
${O_2}^+ + {O_3}^-$	$\rightarrow$	${O_2}^* + {O_3}^*$	3.33E-01	0.0
${O_2}^+ + {O_3}^-$	$\rightarrow$	${O_2}^* + {O_2}^* + O^*$	3.33E-01	0.0
${O_2}^+ + {O_3}^-$	$\rightarrow$	${O_3}^* + O^* + O^*$	3.33E-01	0.0
$O_3 + e^-$	$\rightarrow$	${O_3}^-$	1.00E+00	0.0
$O_3 + O^-$	$\rightarrow$	${O_2}^- + O_2$	1.00E+00	0.0
$O_3 + {O_2}^-$	$\rightarrow$	${O_3}^- + O_2$	1.00E+00	0.0
$O_3 + {O_3}^+$	$\rightarrow$	$O_2 + O_2 + {O_2}^+$	1.00E+00	0.0
${O_3}^- + O^-$	$\rightarrow$	${O_2}^- + {O_2}^-$	1.00E+00	0.0
${O_3}^+ + e^-$	$\rightarrow$	${O_3}^*$	5.00E-01	0.0
${O_3}^+ + e^-$	$\rightarrow$	${O_2}^* + O^*$	5.00E-01	0.0
${O_3}^+ + O^-$	$\rightarrow$	$O^* + {O_3}^*$	5.00E-01	0.0
${O_3}^+ + O^-$	$\rightarrow$	${O_2}^* + {O_2}^*$	5.00E-01	0.0
${O_3}^+ + O_2$	$\rightarrow$	${O_2}^+ + O_3$	4.15E-01	0.0
${O_3}^+ + O_2$	$\rightarrow$	${O_3}^+ + O_2$	8.50E-02	0.0
${O_3}^+ + O_2$	$\rightarrow$	$O_2 + O_2 + O^+$	5.00E-01	0.0
${O_3}^+ + {O_2}^-$	$\rightarrow$	${O_2}^* + {O_3}^*$	3.33E-01	0.0
${O_3}^+ + {O_2}^-$	$\rightarrow$	${O_2}^* + {O_2}^* + O^*$	3.33E-01	0.0
${O_3}^+ + {O_2}^-$	$\rightarrow$	${O_3}^* + O^* + O^*$	3.33E-01	0.0
${O_3}^+ + {O_3}^-$	$\rightarrow$	${O_3}^* + {O_3}^*$	3.33E-01	0.0
${O_3}^+ + {O_3}^-$	$\rightarrow$	${O_3}^* + {O_2}^* + O^*$	3.33E-01	0.0
${O_3}^+ + {O_3}^-$	$\rightarrow$	${O_2}^* + {O_2}^* + {O_2}^*$	3.33E-01	0.0

Appendix B

PLOTS

The contribution of each reaction to the rate of formation of each species in the network as a function of fluence is shown in Figures B.1-B.10. The linestyles plotted refer to different types of reactions given in Table 1, repeated here.

Linestyle	Reaction Type
———	neutral-neutral
- - - - -	ion-neutral
-·-·-·	ion recombination
·····	photoprocesses
-···-··	quenching

Table B.1: Linestyle Legend In the following plots a solid line indicates a neutral-neutral reaction, a dashed line indicates an ion-neutral reaction, a dash-dotted line indicates an ion-ion reaction, a dotted line indicates a photo process and a dash-dot-dot-dotted line indicates a quenching process.

B.1 Neutrals

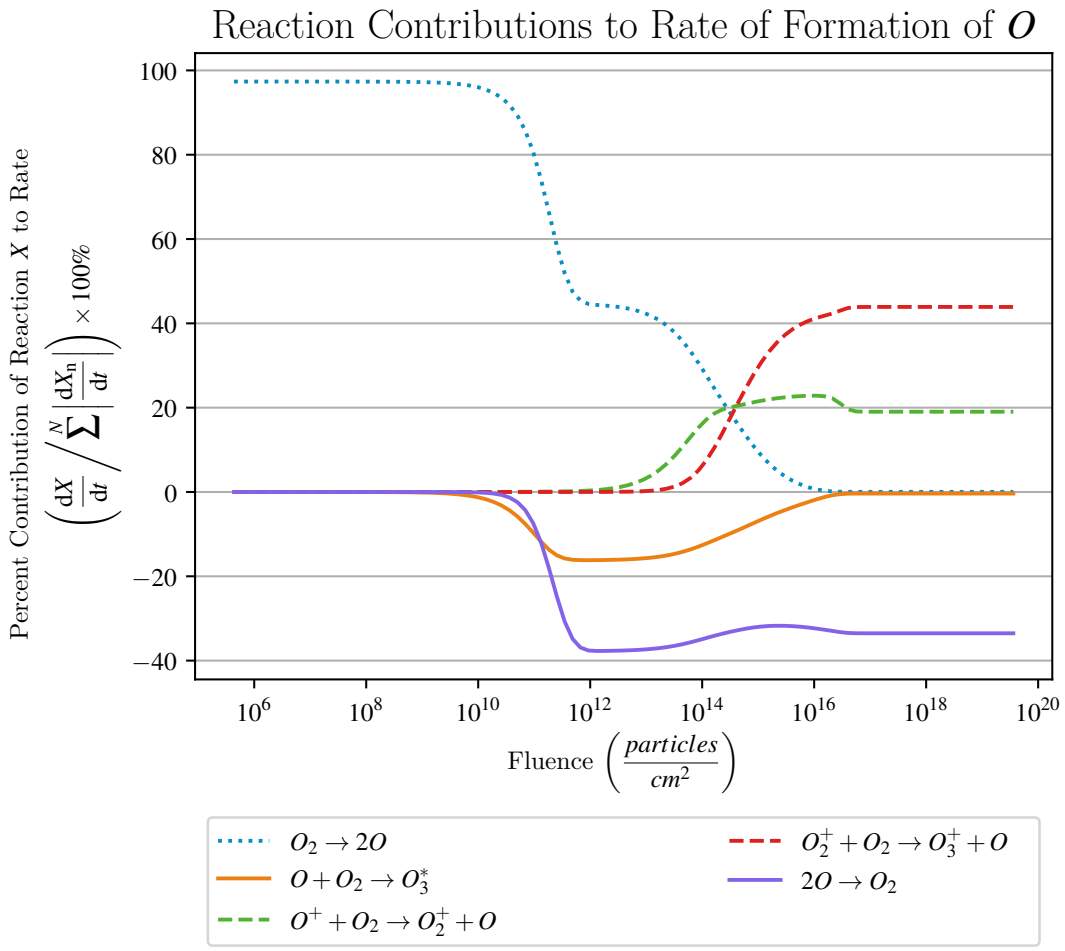

Fig. B.1: Reaction Contributions to the Rate of Formation of O The percent contribution of the indicated reaction to the rate of formation of O with respect to $\log_{10}$ fluence. At early fluences the rate of formation of O is governed by the photoexcitation reaction $O_2 \rightsquigarrow 2O$. As more species form in the ice, the ion-neutral reactions, $O^+ + O_2 \rightarrow {O_2}^+ + O$ and ${O_2}^+ + O_2 \rightarrow {O_3}^+ + O$, become the major formation pathways. The destruction pathways of O during the middle fluences are governed by the neutral-neutral reactions $O + O_2 \rightarrow {O_3}^*$ and $2O \rightarrow O_2$ and the rate contribution of former goes to zero at late fluences.

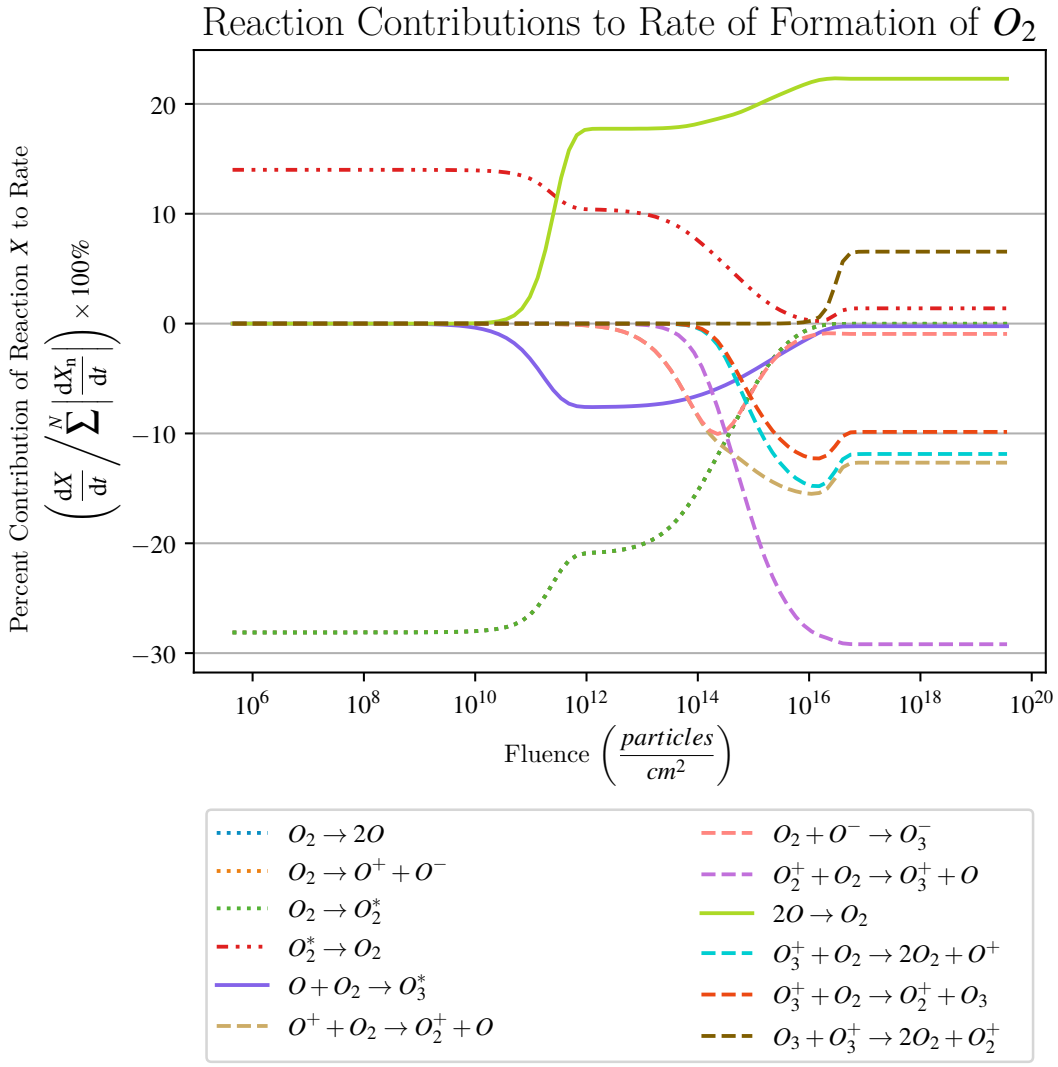

Fig. B.2: Reaction Contributions to the Rate of Formation of O_2 The percent contribution of the indicated reaction to the rate of formation of O_2 with respect to $\log_{10}$ fluence. At the start of our simulations, the ice is composed of entirely O_2 ice. At early fluences the three primary destruction pathways are the photoexcitation/photoionization processes, $O_2 \rightsquigarrow 2O$, $O_2 \rightsquigarrow O^+ + O^-$, and $O_2 \rightsquigarrow O_2^*$. The primary formation pathway at early fluences is the quenching reaction, $O_2^* \rightarrow O_2$. As the cations form in the ice, ion-neutral reactions become the major destruction pathways so that at late fluences the major destruction pathways are $O_2^+ + O_2 \rightarrow O_3^+ + O$, $O^+ + O_2 \rightarrow O_2^+ + O$, $O_3^+ + O_2 \rightarrow 2O_2 + O^+$ and $O_3^+ + O_2 \rightarrow O_2^+ + O_3$. At late fluences the primary formation pathway is the neutral-neutral reaction, $2O \rightarrow O_2$, with the ion-neural reaction, $O_3^+ + O_3 \rightarrow 2O_2 + O_2^+$, contributing non-negligibly to the formation of O_2.

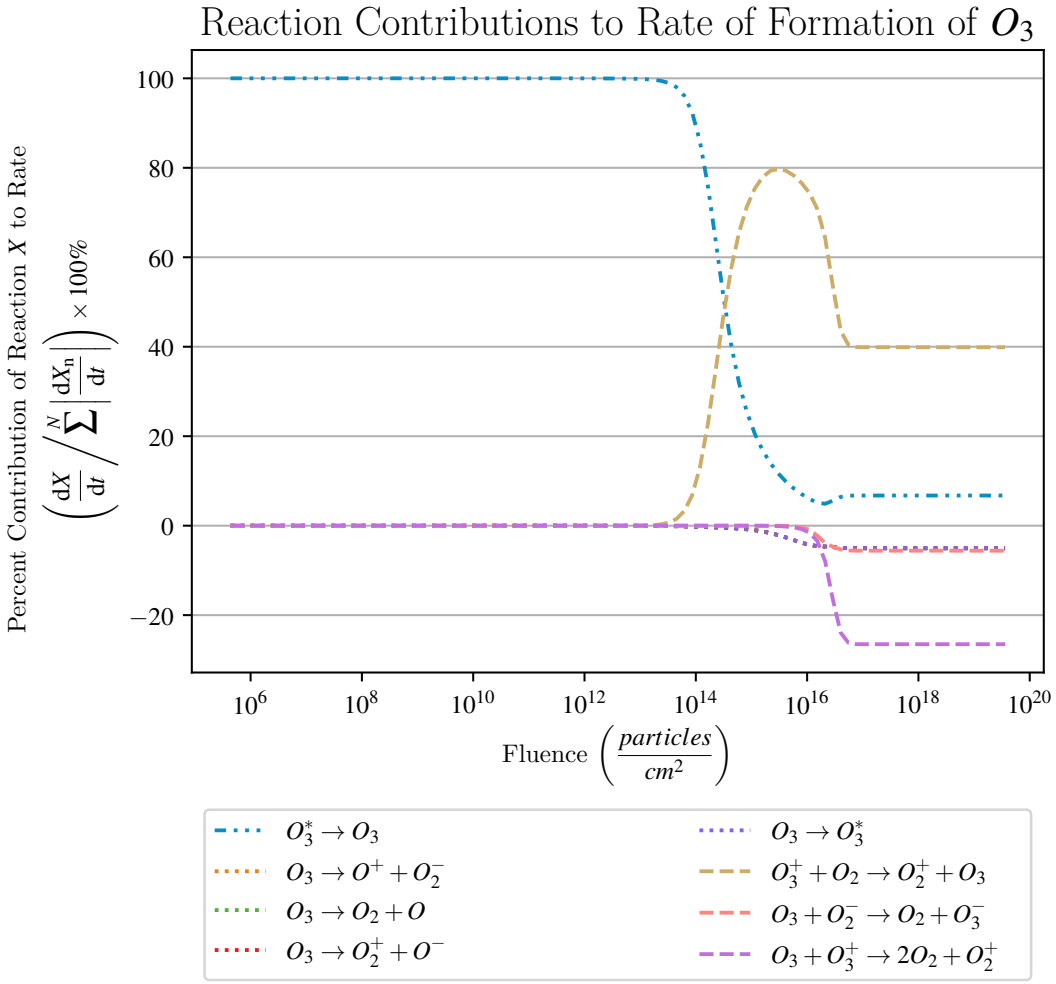

Fig. B.3: Reaction Contributions to the Rate of Formation of O_3 The percent contribution of the indicated reaction to the rate of formation of O_3 with respect to $\log_{10}$ fluence. At early fluences the rate of formation of ozone is governed by the quenching reaction, $O_3{}^* \rightarrow O_3$, where $O_3{}^*$ forms mainly via $O + O_2 \rightarrow O_3{}^*$. However, at middle fluences the ion-neutral reaction, $O_3{}^+ + O_2 \rightarrow O_2{}^+ + O_3$ becomes the major formation pathway. At late fluences, the destruction of ozone is primarily through an ion-neutral pathway, $O_3{}^+ + O_3 \rightarrow 2O_2 + O_2{}^+$, or one of four photoprocesses, $O_3 \rightsquigarrow O^+ + O_2{}^-$, $O_3 \rightsquigarrow O_2 + O$, $O_3 \rightsquigarrow O_2{}^+ + O^-$, or $O_3 \rightsquigarrow O_3{}^*$. Please note that the four photoprocesses are rendered on top of each other; when taken together, account for nearly 20% of the rate.

B.2 Cations

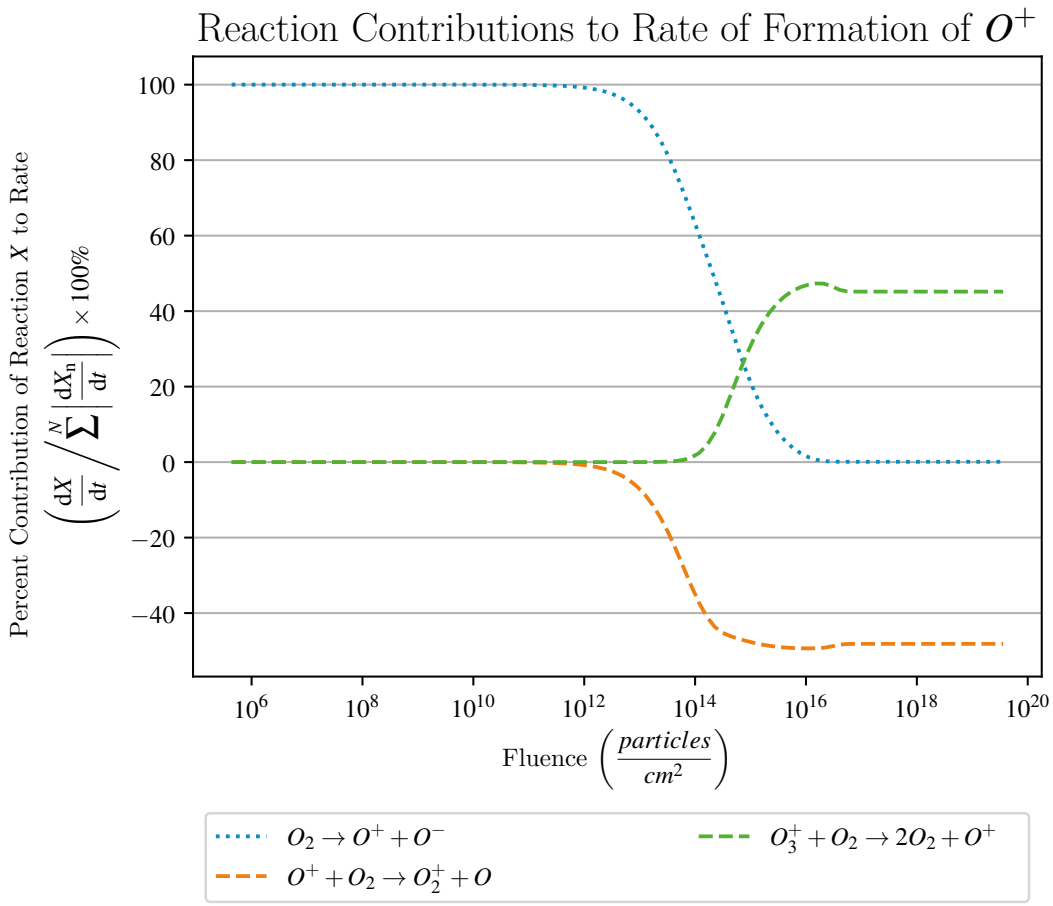

Fig. B.4: Reaction Contributions to the Rate of Formation of O^+ The percent contribution of the indicated reaction to the rate of formation of O^+ with respect to $\log_{10}$ fluence. At early fluences the formation of O^+ is governed by the photoexcitation reaction, $O_2 \rightsquigarrow O^+ + O^-$. At steady state both major formation and destruction pathways are ion-neutral reactions, $O_3{}^+ + O_2 \rightarrow 2O_2 + O^+$ and $O^+ + O_2 \rightarrow O_2{}^+ + O$. Recombination reactions each contribute a negligible ($< 1\%$) amount to the rate.

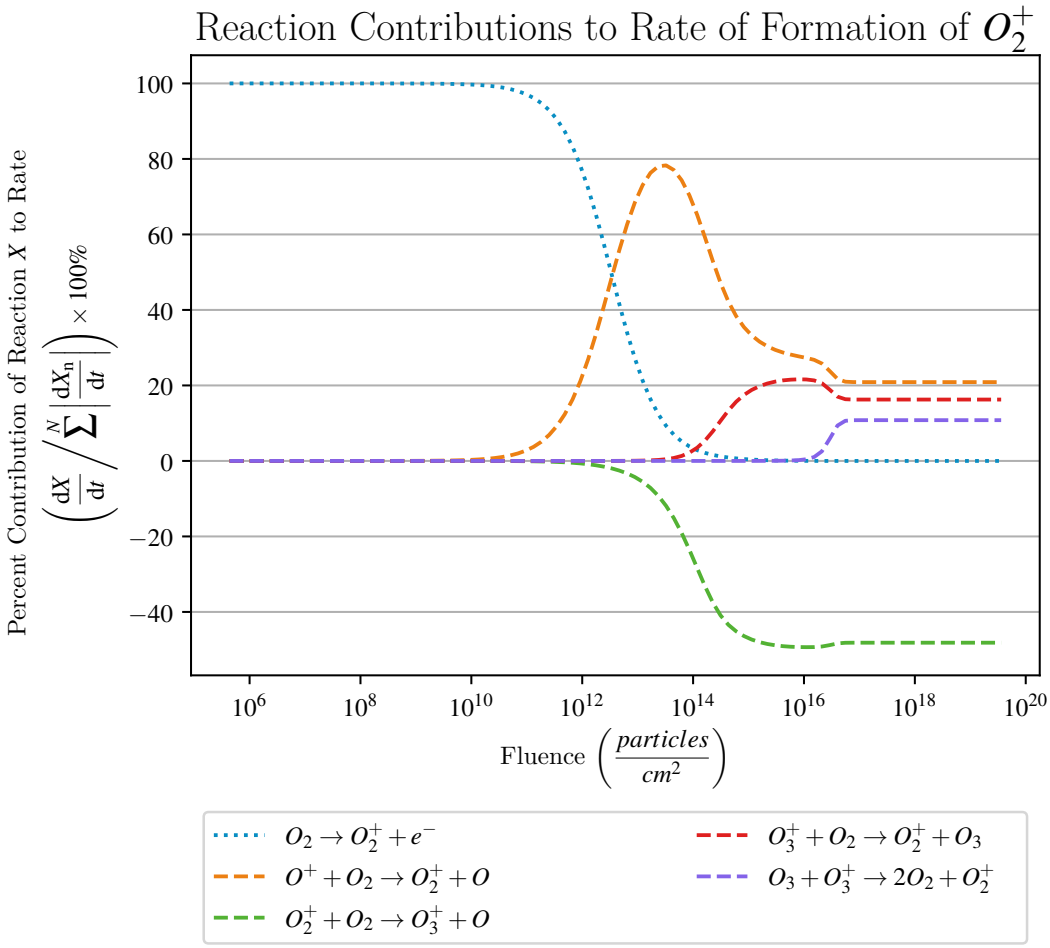

Fig. B.5: Reaction Contributions to the Rate of Formation of O_2^+ The percent contribution of the indicated reaction to the rate of formation of O_2^+ with respect to $\log_{10}$ fluence. At early fluences the formation of O_2^+ is governed by the photoionization reaction, $O_2 \rightsquigarrow O_2^+ + e^-$. At middle and late fluences, all major formation and destruction pathways are ion-neutral reactions, $O^+ + O_2 \rightarrow O_2^+ + O$, $O_3^+ + O_2 \rightarrow O_2^+ + O_3$, $O_3^+ + O_3 \rightarrow 2O_2 + O_2^+$, and $O_2^+ + O_2 \rightarrow O_3^+ + O$. Recombination reactions each contribute a negligible ($< 0.5\%$) amount to the rate.

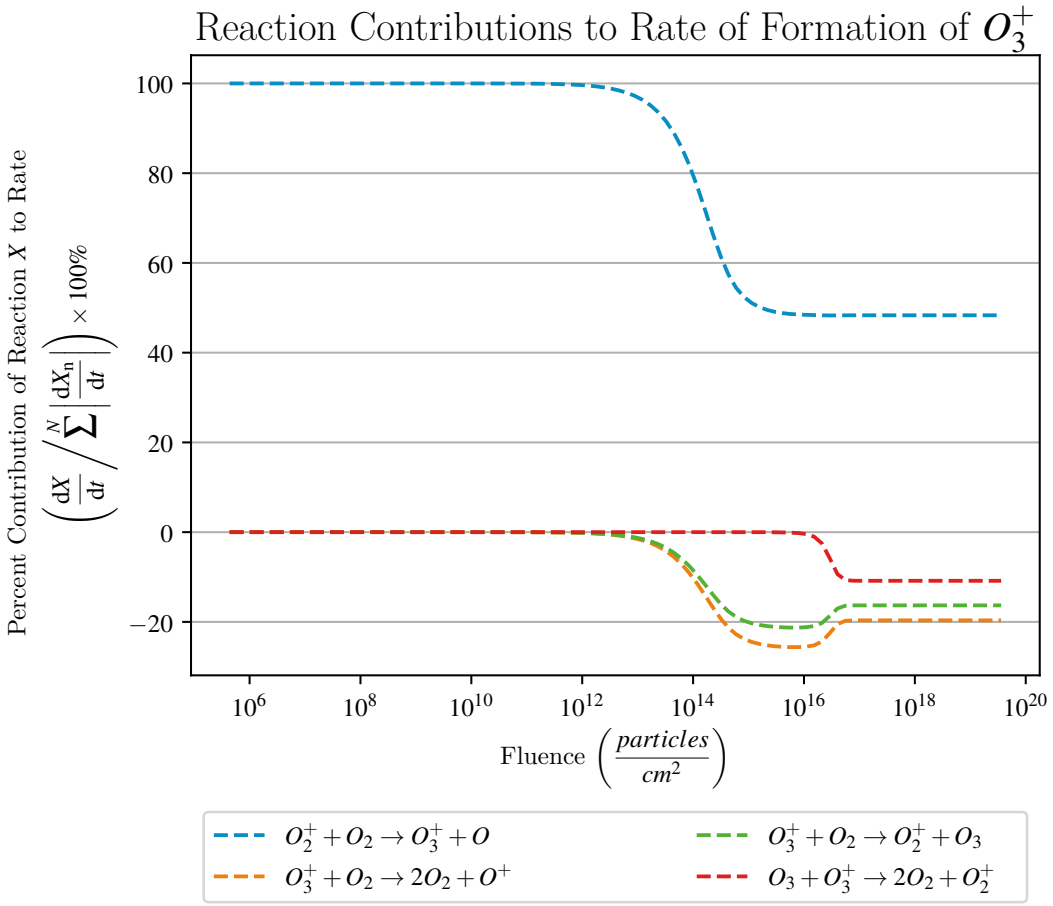

Fig. B.6: Reaction Contributions to the Rate of Formation of O_3^+ The percent contribution of the indicated reaction to the rate of formation of O_3^+ with respect to $\log_{10}$ fluence. At all fluences, ion-neutral reactions are the major formation ($O_2^+ + O_2 \rightarrow O_3^+ + O$) and destruction ($O_3^+ + O_2 \rightarrow 2O_2 + O^+$, $O_3^+ + O_2 \rightarrow O_2^+ + O_3$, and $O_3^+ + O_3 \rightarrow 2O_2 + O_2^+$) pathways of O_3^+. Recombination reactions each contribute a negligible ($< 0.5\%$) amount to the rate.

B.3 Anions

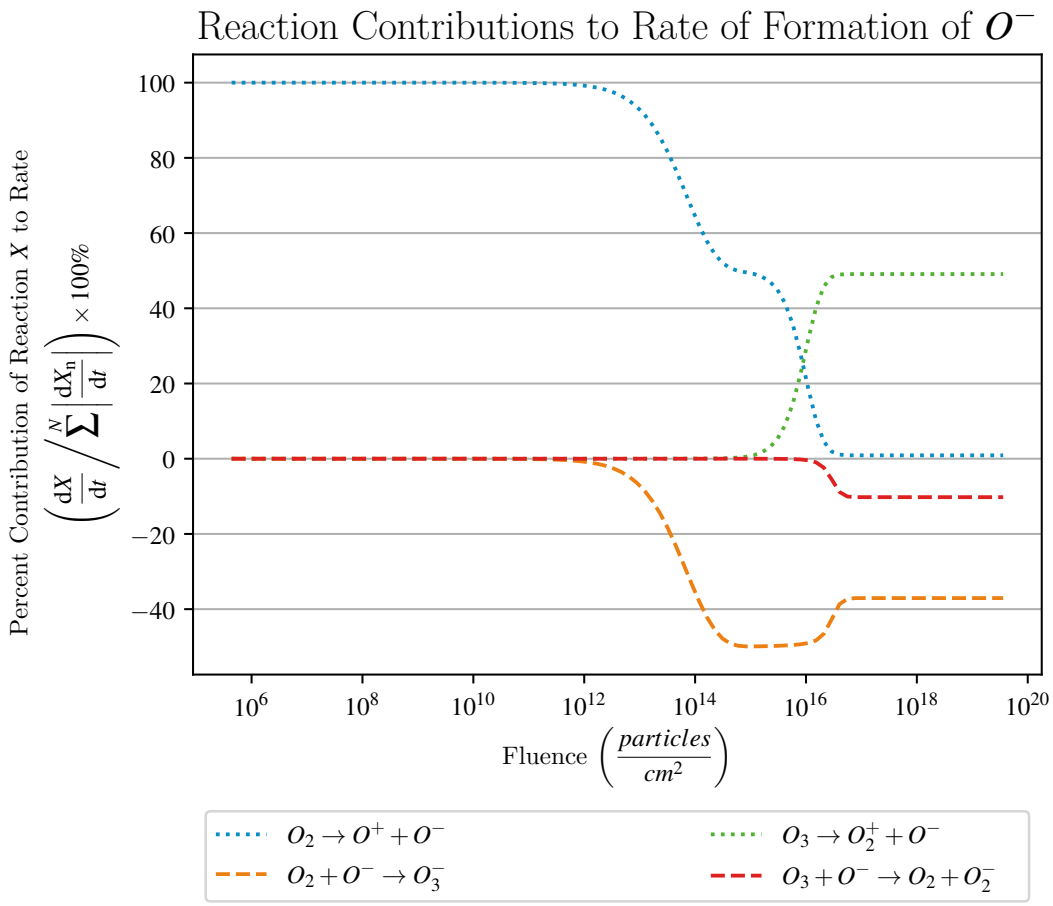

Fig. B.7: Reaction Contributions to the Rate of Formation of O^- The percent contribution of the indicated reaction to the rate of formation of O^- with respect to $\log_{10}$ fluence. The formation of O^- is governed by photoexcitation reactions. At early fluences it is the photodissociation of O_2, $O_2 \rightsquigarrow O^+ + O^-$, but at steady state it is the photodissociation of O_3, $O_3 \rightsquigarrow {O_2}^+ + O^-$. Both major destruction pathways are ion-neutral reactions, $O_2 + O^- \rightarrow {O_3}^-$ and $O_3 + O^- \rightarrow O_2 + {O_2}^-$. Recombination reactions each contribute a negligible ($< 1.3\%$) amount to the rate.

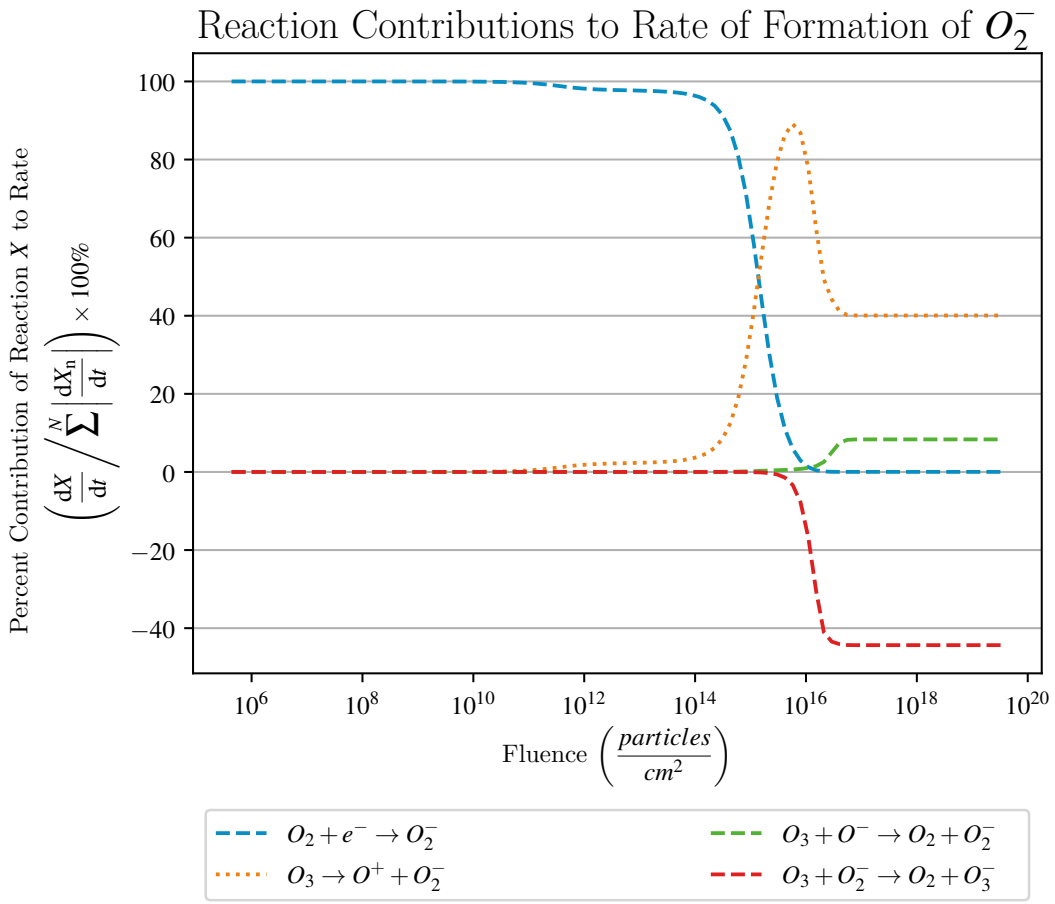

Fig. B.8: Reaction Contributions to the Rate of Formation of O_2^- The percent contribution of the indicated reaction to the rate of formation of O_2^- with respect to $\log_{10}$ fluence. At early fluences O_2^- is formed via the ion-neutral reaction, $O_2 + e^- \rightarrow O_2^-$, but as more species are formed the photodissociation of O_3, $O_3 \rightsquigarrow O^+ + O_2^-$, becomes the major formation pathway. Recombination reactions each contribute a negligible ($< 1.5\%$) amount to the rate.

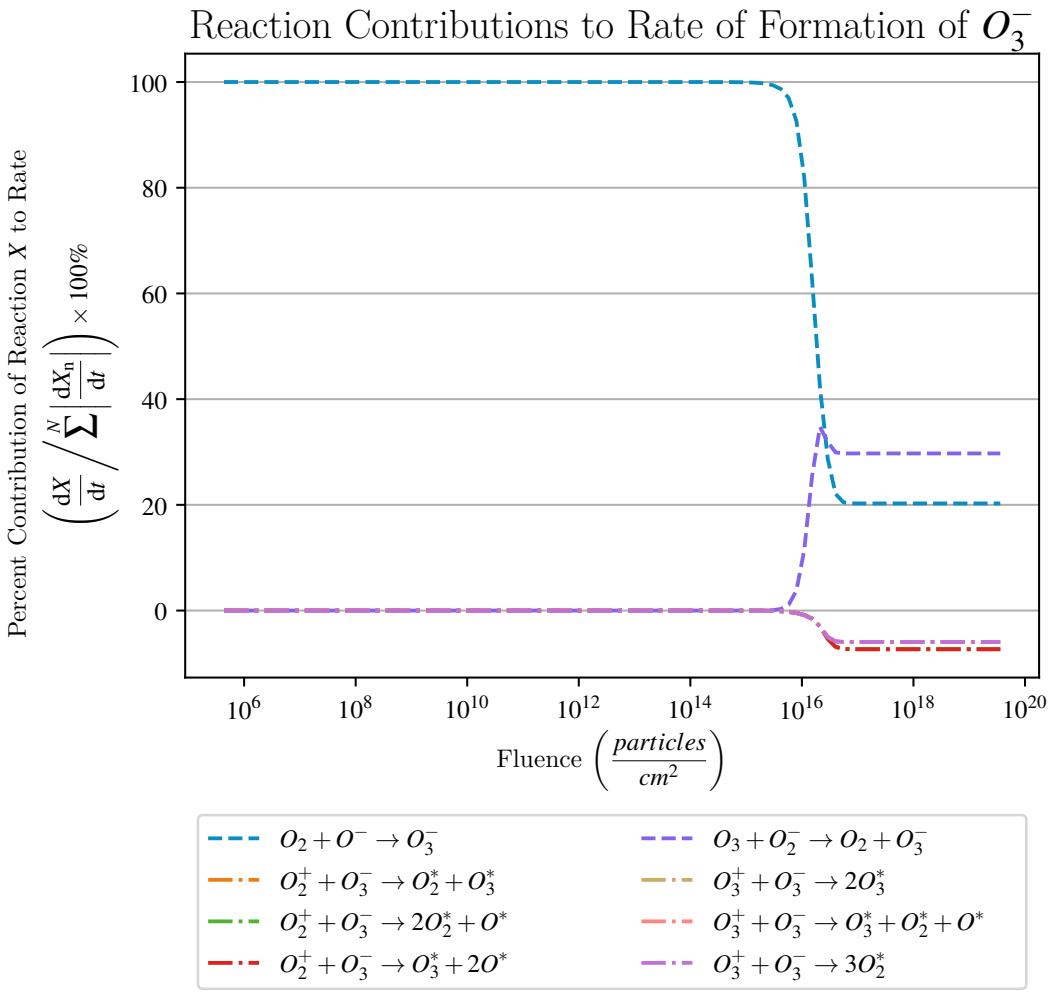

Fig. B.9: Reaction Contributions to the Rate of Formation of O_3^- The percent contribution of the indicated reaction to the rate of formation of O_3^- with respect to $\log_{10}$ fluence. At early fluences O_3^- is formed via the ion-neutral reaction $O_2 + O^- \rightarrow O_3^-$. At late fluences, this reaction accounts for slightly less of the formation than another ion-neutral reaction, $O_3 + O_2^- \rightarrow O_3 + O_3^-$. The destruction of O_3^- occurs entirely through recombination reactions. Please note that the six recombination reactions are plotted on top of each other in the pink and red dash-dotted lines.

B.4 Electrons

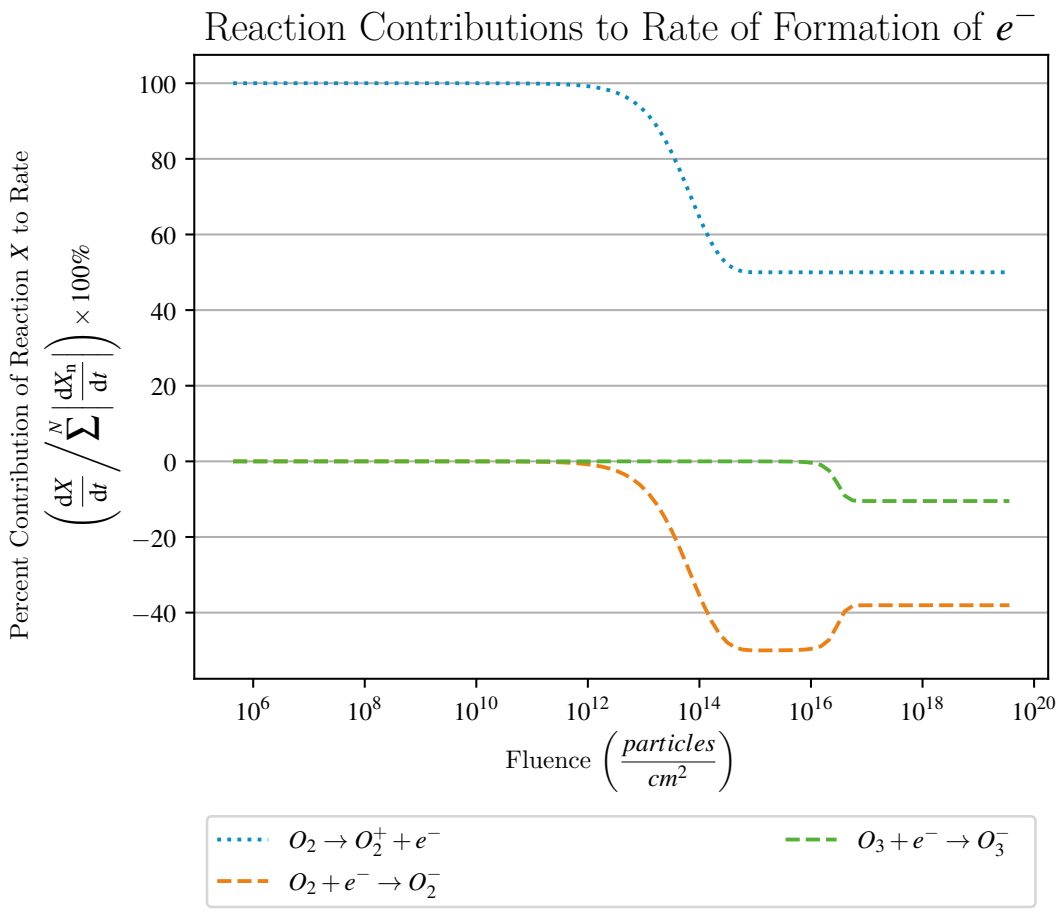

Fig. B.10: Reaction Contributions to the Rate of Formation of e^- The percent contribution of the indicated reaction to the rate of formation of e^- with respect to $\log_{10}$ fluence. Electrons are entirely produced in the photoionization of O_2, $O_2 \rightsquigarrow O_2{}^+ + e^-$. They are consumed in ion-neutral reactions with O_2 and O_3. Recombination reactions each contribute a negligible ($< 0.5\%$) amount to the rate.